Multiphysics modeling of volcanic unrest at Mt. Ruapehu (New Zealand)

Fee Arens[1], Armando Coco[2], Joachim Gottsmann[1], James Hickey[3], Geoff Kilgour[4]

[1]School of Earth Sciences, University of Bristol, Bristol, UK
[2]Department of Mathematics and Computer Science, University of Catania, Italy
[3]Department of Earth and Environmental Sciences, University of Exeter, Cornwall, UK
[4]GNS Science, Wairakei Research Center, Taupo, New Zealand

Key Points:

- Multiphysics simulations to study unrest processes at Mt. Ruapehu
- Spatio-temporal variations in self-potential and gravity changes identified as indicators of magmatic unrest
- Hydrothermal unrest induces resolvable ground displacements, and changes in gravity and self-potential

Corresponding author: Fee Arens, `fee.arens@bristol.ac.uk`

Abstract

Pre-eruptive signals at the crater lake-bearing Mt. Ruapehu (New Zealand) are either absent or hard to identify. Here, we report on geophysical anomalies arising from hydrothermal unrest (HTU) and magmatic unrest (MU) using multiphysics numerical modeling. Distinct spatio-temporal anomalies are revealed when jointly solving for ground displacements and changes in gravitational and electrical potential fields for a set of subsurface disturbances including magma recharge and anomalous hydrothermal flow. Protracted hydrothermal injections induce measurable surface displacements (> 0.5 cm) at Ruapehu's summit plateau, while magmatic pressurization (5 - 20 MPa) results in ground displacements below detection limits. Source density changes of 10 kg/m^3 (MU simulations) and CO_2 fluxes between 2150 and 3600 t/d (HTU simulations) induce resolvable residual gravity changes between +8 and -8 μGal at the plateau. Absolute self-potential anomalies are predicted to vary between 0.3 mV and 2.5 mV for all unrest simulations and exceed the detection limit of conventional electric surveying. Parameter space exploration indicates that variations of up to 400% in the Biot-Willis coefficient produce negligible differences in surface displacement in MU simulations, but strongly impact surface displacement in HTU simulations. Our interpretation of the findings is that monitoring of changes in self-potential and gravity should permit insights into MU at Ruapehu, while HTU is best characterised using ground displacements, residual gravity changes and self-potential anomalies. Our findings are useful to inform multiparameter monitoring strategies at Ruapehu and other volcanoes hosting crater lakes.

Plain Language Summary

Eruptions at Mt. Ruapehu in New Zealand often occur without any warning amid an absence of what are called pre-eruptive geophysical signals. In order to study the detectability of relevant geophysical signals, we use physics-based models to simulate two distinct subsurface processes at Mt. Ruapehu: magma accumulation and flow of hydrothermal fluids. Both processes involve fluid flow, density variations and pressure changes in the ground and have the potential to trigger eruptive activity. Here we identify distinct measurable sets of geophysical signals from either subsurface process: changes in the electrical and gravitational potential fields, or surface deformation. Our study highlights the benefit of computer models to provide useful information on the link between subsurface processes and measurable geophysical signals prior to eruptive activity. Our findings may have implications for volcano monitoring efforts at Mt. Ruapehu and other crater lake volcanoes.

1 Introduction

Episodes of magmatic, hydrothermal or hybrid unrest are usually characterised by anomalous geophysical observations. For example, geodetic anomalies during hydrothermal unrest result from the circulation of multi-phase and multi-component fluids and concurrent thermo-poroelastic responses (e.g., Bonafede, 1991; Hutnak et al., 2009; Fournier & Chardot, 2012), while geodetic signals during magmatic unrest arise from mass and density variations in the sub-volcanic plumbing system (Lisowski, 2006; Currenti, 2014). Hybrid unrest is caused by the modulation of subsurface stresses and strains from magma rejuvenation by poroelastic responses in volcano-hydrological reservoirs (e.g., aquifers, hydrothermal systems; Strehlow et al. (2015); Newhall et al. (2001); Shibata and Akita (2001); Strehlow et al. (2020)). Furthermore, strain-induced fluid flow caused by poroelastic responses to magmatic stressing or ascending hydrothermal fluids generate self-potential (SP) anomalies (Arens et al., 2020; Corwin & Hoover, 1979; Zlotnicki & Nishida, 2003; Revil, Naudet, et al., 2003).

Volcanic risk assessment and eruption forecasting necessitates the characterisation of the nature of unrest and the discrimination between magmatic and hydrothermal contributions (Todesco & Berrino, 2005; Rouwet et al., 2014; Jasim et al., 2015). Multi-parameter geophysical studies help to identify driving mechanisms and source properties behind volcanic unrest, especially when interpretations of field observations are combined with data modelling (e.g., Wauthier et al., 2016; Gottsmann et al., 2008; Gottsmann, Flynn, & Hickey, 2020; Hickey et al., 2016; Zhan et al., 2021; Rinaldi et al., 2011). Joint ground displacement and gravity change time series have, for example, been used at several volcanoes to interrogate enigmatic unrest processes (Gottsmann, Biggs, et al., 2020; Coco, Gottsmann, et al., 2016; Currenti & Napoli, 2017; Zhan et al., 2019). While ground deformation monitoring (Sparks et al., 2012) is common at many restless volcanoes, monitoring of gravimetric and electrical potential field changes is scarce, despite joint inversion of multiphysics data sets such as from seismic and SP investigations providing useful information on the timing and evolution of different source mechanisms (Mahardika et al. (2012); Zlotnicki (2015) and references therein). Here we present a suite of multiphysics models which jointly and simultaneously solve for ground displacements and gravitational and electrical potential field changes arising from magmatic and hydrothermal unrest processes. We test for the detectability of unrest signals and focus our study on Mt. Ruapehu in New Zealand, a volcano with a recent history of enigmatic unrest episodes which might herald renewal of eruptive activity.

2 Geological background and motivation

Mt. Ruapehu is a large stratovolcano of dominantly andesite composition and one of New Zealand's most active volcanoes. This volcano is North Island's highest peak at 2797 m a.m.s.l. and it hosts three ski fields, which during winter months, hosts thousands of recreational users. Ruapehu is located in the Tongariro National Park (TNP), alongside two other active andesitic volcanoes (Ngauruhoe and Tongariro), the Tongariro Volcanic Centre forms the southwestern edge of the Taupo Volcanic Zone (TVZ; G. N. Kilgour et al. (2013); Rowlands et al. (2005); C. A. Miller et al. (2020)). The TVZ is a NNE-trending rifted arc basin resulting from oblique, westward subduction of the Pacific Plate beneath the Australian Plate (Cole, 1990).

Volcanism at Ruapehu has been active for the past $\sim$ 250 ka (Gamble et al., 2003) with eruptive activity resulting from hydrothermal or magmatic perturbations, or a combination of both. Hydrothermal unrest is thought to be provoked by the pulsating ascent of heat and magmatic fluids through the active hydrothermal system which feeds Ruapehu's acid crater lake (Te Wai *ā*-Moe in M*ā*ori; Hurst et al. (1991); Christenson and Wood (1993); Jones et al. (2008); Leonard et al. (2021)). Beneath the lake, geophysical (Rowlands et al., 2005; Ingham et al., 2009; Jones et al., 2008) and petrological (G. N. Kilgour et al., 2013) studies highlight a transcrustal mush zone within which distinct compositional magma batches are believed to reside (Nakagawa et al., 1999, 2002; G. N. Kilgour et al., 2013). It has been proposed that magmatic unrest might be triggered by the interaction of recharge from deeper reservoirs with remnant magmas stored in the crustal mush zone (Conway et al., 2020; Nakagawa et al., 1999; Gamble et al., 1999; G. N. Kilgour et al., 2014) with the potential to culminate in an eruption.

Recent eruptive activity at Ruapehu has ranged from small, frequent phreatic explosions (G. Kilgour et al., 2010; Houghton et al., 1987), through phreato-magmatic eruptions from the crater lake (Houghton et al., 1987) to magmatic eruptions, such as in 1945, 1995 and 1996 (Nairn et al., 1979; Christenson, 2000). Eruptive activity at Ruapehu entails a variety of hazards including ballistics, Surtseyan jets, lahars and ash fallout (e.g., Bryan & Sherburn, 1999; G. Kilgour et al., 2010; Nakagawa et al., 1999). While elevated seismicity, and changes in lake temperature and water level accompany volcanic unrest (Leonard et al., 2021), magmatic and hydrothermal eruptions frequently occur without early, protracted or identifiable precursors (e.g., Mordret et al., 2010; Jolly et al., 2010; Sherburn et al., 1999). The absence of reliable precursory geophysical signals at this very-high threat volcano (C. Miller & Jolly, 2014) poses a problem for hazard assessment and risk mitigation at the popular TNP and surrounding areas. In this study, we simulate magmatic or hydrothermal unrest at Ruapehu in order to interrogate emerging surface geophysical signals as indicators of unrest processes and their nature with a view to inform recommendations for monitoring protocols at the volcano.

3 Methodology

We use numerical forward modelling to quantify geophysical observables from (i) magmatic and (ii) hydrothermal unrest at Mt. Ruapehu. Magmatic unrest (MU) is simulated by the pressurisation of Ruapehu's transcrustal mush zone by magma injection. Resultant changes in subsurface stress and strain trigger a poroelastic response in the overlying hydrothermal system (HTS) and edifice. Strain-induced fluid flow of water generates self-potential anomalies from electrokinetic processes, while mass and volume changes trigger ground displacements and gravity changes. Hydrothermal unrest (HTU) is simulated by injecting hot multi-phase and multi-component fluids (CO_2, H_2O) at the bottom of Ruapehu's HTS. Pore pressure and temperature changes trigger thermo-poroelastic responses in the HTS and edifice observable by ground displacements and changes in the gravitational and electrical potential fields. In this study, processes triggering MU and HTU are modelled in isolation to study geophysical fingerprints resulting from either unrest with the aim to identify key geophysical observables. The simulations solve different equations described next.

3.1 Physical processes

3.1.1 Strain-induced fluid flow

For a single-phase fluid, strain-induced flow through a water-saturated porous rock can be described by Darcy's law:

$$\mathbf{v} = -\frac{\kappa}{\eta_f}(\nabla p_f - p_0), \tag{1}$$

with $\mathbf{v}$ being the Darcy velocity, κ being the permeability of the porous rock, η_f being the fluid's viscosity, p_f being the pore pressure and p_0 the initial pore pressure distribution. Driving forces for fluid flow are temporal strain changes ($\frac{\partial \epsilon_{vol}}{\partial t}$) in the subsurface (Biot, 1962; Wang, 2000):

$$q - \rho_f \alpha_{BW} \frac{\partial \epsilon_{vol}}{\partial t} = \rho_f S_{PE} \frac{\partial p_f}{\partial t} + \nabla \cdot (\rho_f \mathbf{v}), \tag{2}$$

where q is the mass source/sink, ρ_f is the fluid density, and ϵ_{vol} is the volumetric strain. S_{PE} is the poroelastic storage ($S_{PE} = \Phi\chi_f + \frac{(\alpha_{BW}-\Phi)(1-\alpha_{BW})}{K}$) with Φ the porosity of the medium , χ_f the fluid's compressibility and K the bulk modulus. Equations 1-2 denote the solid-to-fluid coupling and are solved for MU simulations solely.

3.1.2 Hydrothermal model

The simulation of hydrothermal unrest is based on the flow of fluid and heat in a porous medium by solving a set of mass and energy balance equations which are described as follows (see Pruess et al. (1999); Xu et al. (2004) for further reading):

$$\frac{\partial Q_\alpha}{\partial t} + \nabla \cdot \mathbf{F}_\alpha - q_\alpha = 0 \qquad \alpha = 1, ...m, N, \tag{3}$$

with $\mathbf{F}$ being the flux, q being the source/sink term and Q being the accumulation term for m mass components (H_2O and CO_2, $\alpha = 1, 2$ hence m = 2) and the energy equation ($\alpha = N$). Accumulation term (Q_α) and fluid fluxes for the mass balance equation are defined as follows:

$$Q_\alpha = \Phi \sum_\beta \rho_\beta S_\beta \chi_\beta^\alpha \qquad \mathbf{F}_\alpha = \sum_\beta \chi_\beta^\alpha \mathbf{v}_\beta, \tag{4}$$

with the subscript β =l or g characterising the liquid and gas phase, respectively, with the permeability κ_β, the density ρ_β, the saturation S_β and the mass fraction χ^α_β of component m in phase β. Mass fluxes $\mathbf{F}_\alpha$ can be calculated by using the extended Darcy's law for multi-component and multi-phase fluid flow:

$$\mathbf{v}_\beta = -\kappa \frac{\kappa_{r\beta}\rho_\beta}{\eta_\beta}\Bigg(\nabla p_\beta - \rho_\beta \mathbf{g}\Bigg), \tag{5}$$

with the Darcy's velocity $\mathbf{v}_\beta$ in phase β , the relative permeability $k_{r\beta}$ and the gravitational acceleration vector $\mathbf{g}$. All other parameters are equivalent to the single-phase fluid, but accounting for different phases (β =l or g).

For the energy equation, the accumulation term (Q_N) and heat flux (F_N) are defined as:

$$Q_N = \Phi \sum_\beta \rho_\beta e_\beta S_\beta + (1-\Phi)\rho c_p T \qquad \mathbf{F}_N = -\lambda \nabla T + \sum_\beta h_\beta \mathbf{v}_\beta, \tag{6}$$

where e_β is the specific internal energy and h_β the specific enthalpy in phase β, T is the temperature and ρ, cp and λ are the density, heat capacity and thermal conductivity of the porous medium, respectively.

3.2 Observables

Our study focuses on ground displacement, gravity changes and self-potential signals as described below. We test for the detectability of modelled signals, with common GNSS surveys at Ruapehu resolving ground displacements of 0.5 cm horizontally to 1 cm vertically (Mordret et al., 2010). Gravity changes at the 5μGal level are resolvable with carefully executed standard survey protocols (Battaglia et al., 2008) and the detectability of SP observations ranges between a few and 100 microvolts (μV), with most field equipment resolving 0.1 mV (Revil & Jardani, 2013; Zlotnicki, 2015; Crespy et al., 2008).

3.2.1 Ground displacement

In areas where rocks are in quasi-static equilibrium (deformation processes occur slowly), displacement resulting from thermo-poroelastic responses can be derived from Hooke's law coupled with pressure and temperature effects (Fung, 1965; McTigue, 1986; Rice & Cleary, 1976):

$$\begin{aligned} \nabla \cdot \sigma_b &= 0, \\ \sigma_b &= \mathbf{C}\epsilon - \alpha_T K \Delta T \mathbf{I} - \alpha_{BW} \Delta p_f \mathbf{I}, \\ \epsilon &= \frac{1}{2}(\nabla \mathbf{u} + (\nabla \mathbf{u})^T), \end{aligned} \tag{7}$$

with the stress σ_b and strain ϵ tensor, the displacement vector $\mathbf{u}$ and the identity matrix $\mathbf{I}$. The elasticity matrix $\mathbf{C}$=$\mathbf{C}$(E,ν) and bulk modulus ($K = \frac{E}{3(1-2\nu)}$) are represented by the Young's modulus (E) and the Poisson's ratio (ν). The first term on the right hand side of equation 7 represents Hooke's law of linear elasticity, while the second and third term account for stress and strain variations resulting from temperature (ΔT) and pore pressure (Δp_f) changes, respectively. Key parameters for thermo-poroelastic response are the volumetric thermal expansion coefficient α_T and Biot-Willis coefficient α_{BW}. For MU simulations, we fully couple poroelastic responses with stress and strain changes affecting fluid flow and vice versa, while HTU simulations represent a one-way-coupling, where temperature and pressure changes control deformation process but not vice versa.

In volcanic areas where magmatic reservoirs heat surrounding rocks, viscoelastic behaviour most appropriately characterises time-dependent deformation processes (Del Negro et al., 2009). Therefore, we invoke a temperature-dependent viscoelastic rheology (see

Supplementary Material section S1 and Fig. S1) of the crust in the MU model by solving stress-strain relations using a Standard Linear Solid (SLS) parameterization (Del Negro et al., 2009; Hickey & Gottsmann, 2014; Hickey et al., 2016), which is most representative for crustal material (Head et al., 2019, 2021). The SLS model consists of an elastic branch controlled by the shear modulus G and a viscoelastic branch characterised by the relaxation time τ_0:

$$\tau_0 = \frac{\eta_r}{G}, \tag{8}$$

with the shear viscosity η_r. Both branches are split equally using the fractional components ($\mu_1 = \mu_0 = 0.5$) of G. The shear viscosity is derived using the Arrhenius approximation:

$$\eta_r = A \cdot e^{\frac{H}{RT}}, \tag{9}$$

where A is the Dorn parameter (A=10^9 Pa s), H is the activation energy (H=120000 J mol^{-1}), R is the gas constant (R=8.314 J mol^{-1} K^{-1}) and T is the temperature. In our parameterization, near-elastic behaviour of rocks (over timescales relevant for the study) occur in volumes of low temperature such as the edifice.

3.2.2 Gravity changes

Gravity changes at volcanoes are attributed to subsurface density changes $\Delta\rho(x, y, z)$ resulting from the redistribution of hydrothermal fluids (e.g., Todesco et al., 2010; Rinaldi et al., 2011; Currenti & Napoli, 2017) or magma, and shifting of density boundaries by concurrent ground deformation. (Bonafede & Mazzanti, 1998; Currenti, 2014; Gottsmann, Biggs, et al., 2020). Gravity changes Δg are calculated by solving the Poisson's equation for the gravitational potential ϕ_g (Cai & Wang, 2005):

$$\nabla^2\phi_g = -4\pi G\Delta\rho(x, y, z), \quad with \quad \Delta g(x, y, z) = -\frac{\partial\phi_g}{\partial z}, \tag{10}$$

where G is the gravitational constant. By imposing Dirichlet boundary conditions of zero at infinity the mathematical problem is closed.

Subsurface density changes for MU simulations consist of three source terms and can be calculated as follows (Bonafede & Mazzanti, 1998; Currenti, 2014; Zhang et al., 2004):

$$\Delta\rho(x, y, z) = -\mathbf{u} \cdot \nabla\rho_r + \Delta\rho_m - \rho_r\nabla\mathbf{u}, \tag{11}$$

with the density of the medium ρ_r and the source density change $\Delta\rho_m$. The first term on the right-hand side results from the displacements of subsurface density boundaries. The second term quantifies density variations in the transcrustal magma reservoir due to influx of new mass, controlled by the contraction of resident magma and the reservoir expansion. The third term accounts for the compressibility of the surrounding rock (Bonafede & Mazzanti, 1998).

Density variations from fluid redistribution in HTU simulations are calculated with respect to the initial fluid density distribution (ρ_0; Coco, Currenti, et al. (2016); Currenti and Napoli (2017)):

$$\Delta\rho = \rho_k - \rho_0, \quad with \quad \rho_k = \Phi\sum_\beta \rho_\beta S_\beta, \tag{12}$$

for each time step (k), using the fluid density and saturation in phase β.

We derive residual gravity changes from $\delta g_r(x, y, z) = -\frac{\delta\phi_g}{\delta z} - \gamma w$, where -$\gamma w$ is the free-air effect, with the vertical displacement w and the theoretical Free-Air gradient (-308.6 μGal/m).

3.2.3 Self-potential

Self-potential (SP) anomalies in porous media arise from the drag of excess charge with the fluid flow (electrokinetic processes, e.g., Revil and Florsch (2010); Revil et al.

(2012)). Here, we couple SP signals to pore pressure changes in response to strain-induced fluid flow (MU) or the injection of a hot multi-phase and multi-component fluid (HTU). The total current density (**j**) resulting from electrokinetic processes is calculated as follows (see Sill (1983); Revil, Pezard, and Glover (1999); Revil, Schwaeger, et al. (1999); Bolève et al. (2011) for details):

$$\mathbf{j} = -\sigma \nabla \varphi - L_{SP} \nabla p_f, \tag{13}$$

where σ is the electrical conductivity of the medium, φ the electrical potential, p_f the pore pressure and L_{SP} the streaming current coupling coefficient. The latter is related to the streaming-potential coupling coefficient (C_{SP}) via $L_{SP} = -C_{SP}\sigma$, whereby C_{SP} is a key parameter to quantify hydro-electric mechanisms. Applying the continuity equation for electrical charge ($\nabla \cdot \mathbf{j} = 0$) to equation 13 yields the Poisson's equation:

$$\nabla \cdot (\sigma \nabla \varphi) = \Im, \tag{14}$$

where $\Im$ is the volumetric current source density defined as $\Im = -\nabla \cdot (L_{SP} \nabla p_f)$. An electrical reference potential is set to zero at an arbitrary point, as the electrical potential is a relative measure.

3.3 Model implementation

We develop a suite of 2D axisymmetric forward models to simultaneously solve for ground displacement, self-potential and gravity changes at Mt. Ruapehu by magmatic and hydrothermal unrest. All numerical models incorporate topography as well as subsurface mechanical and hydro-electric heterogeneity (see Tab. 2).

3.3.1 Magmatic unrest model

We simulate magmatic unrest using the commercial Finite-Element Analysis package COMSOL Multiphysics (Version 5.3). Figure 1 shows the model geometry and domain size with a radial (r) and vertical extent (z) of 50 km and 75 km, respectively. The crust (z < 0 km) and the edifice (z ≥ 0 km) make up the main domains. The edifice above 1.5 km a.m.s.l. (Fig. 1b) is divided into three sub-domains representing the hydrothermal system (HTS, r = 0 - 50 m), the transition zone (TZ, r = 50 - 150 m) and the edifice (r > 150 m), respectively.

A vertically extended mush zone is proposed to be located between 2-9 km depth below mean sea level (Rowlands et al., 2005; Ingham et al., 2009; Jolly et al., 2010; G. N. Kilgour et al., 2013). We represent this mush zone as a prolate ellipsoidal domain embedded in a viscoelastic crust. The semi-axes of the ellipsoid are derived to match reservoir volume estimates from previous eruptive volumes following Browning et al. (2015) (see section S2). See Table S2 for the reservoir geometry of a maximum dense rock equivalent (DRE) eruptive volume of $3{\cdot}10^7$ m^3 (G. Kilgour et al., 2010) with a reference tensile strength of 10 MPa. The injection of new magma into a transcrustal reservoir can trigger pressurization and density changes (e.g., Browning et al., 2015; Gudmundsson, 2006; Gottsmann et al., 2003). In the absence of precise data, we allocate a source pressure change (ΔP) of 10 MPa to the boundaries of the mush zone with ΔP matching the tensile strength of the crust (T_0 = 10 MPa) as proposed by Gudmundsson (2012). Furthermore, we assign a density change of 10 kg/m^3 to the mush zone resulting from the intrusion of relatively high-density magma into Ruapehu's mush zone as proposed by G. Kilgour et al. (2010); Nakagawa et al. (1999). To account for instantaneous source pressurization and density changes, we stepped ΔP and $\Delta\rho_m$ at t = 10^{-6}d, while ΔP and $\Delta\rho_m$ are kept constant thereafter. Solid mechanics and gravity changes are modelled in the crust and edifice, while an additional domain above the free surface is required to simulate gravity changes (Fig. 1a). Boundary conditions for the solid mechanics solver are a free surface along the edifices topography, roller conditions (free of vertical displacement) at the right boundary, a fixed bottom boundary and a symmetry axis on the left

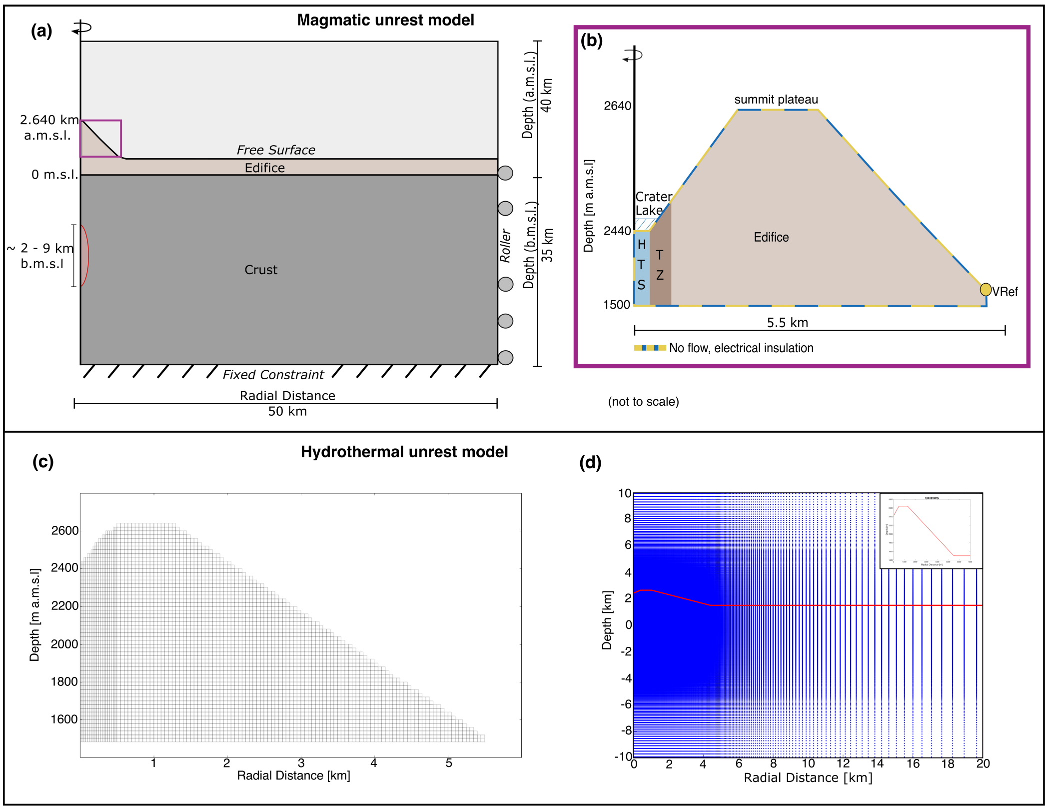

Figure 1. Illustration of the 2D asymmetric model setup for magmatic unrest (MU; upper panels) and hydrothermal unrest (HTU; lower panels) simulations. (a) The mush zone (red ellipsoid) is embedded in a viscoelastic crust located at a centre depth of z = - 5.5 km on the symmetry axis. Boundary conditions for solid mechanics are also shown. The edifice above z $\geq$ 1.5 km (b) is divided into the hydrothermal system (HTS), the transition zone (TZ) and the edifice, in which poroelastic and electric processes are simulated. A no-flow and electric insulation boundary surrounds these domains, while internal boundaries are treated as continuous. An electrical reference potential (V_{Ref}=0) is applied at r = 5.5 km (yellow circle). Ruapehu's crater lake is shown for representation but is excluded in the numerical models. The lower panels show the meshes for HTU simulations, with the TOUGHREACT model being confined to the edifice (c). The electro-mechanical model dimension (d) is extended radially and vertically, with the red line representing Ruapehu's topography. Model domains for HTU simulations are equivalent to the MU model setup.

side. Dirichlet boundary conditions for gravity changes are set to zero at the outer boundaries.

We solve poroelastic responses and strain-induced self-potential anomalies in the sub-domains (HTS, TZ, edifice) above 1.5 km a.m.s.l. using the approaches proposed in (Strehlow et al., 2015; Arens et al., 2020). The initial pore pressure distributions for strain-induced fluid flow at t = 0 is taken from the background HTU simulation (see section 3.3.2). Boundary conditions are no-flow and an electric insulation with an electrical reference potential of φ=0 V applied at r = 5.5 km and z = 1.52 km as the electrical potential is relative to a reference point. All internal boundaries for solid mechanics, gravity changes, poroelasticity and electrokinetics are continuous.

3.3.2 Hydrothermal unrest model

We use the TOUGHREACT code (Xu et al. (2004); Pruess et al. (1999), EOS2 module) to simulate hydrothermal unrest at Ruapehu by solving for heat and mass transport in porous media, but neglect reactive transport. The HTU model geometry (Figure 1c) is confined to the edifice (z$\geq$1.5 km a.m.s.l and r < 5.5 km) with model domains being equivalent to the MU model setup. The HTS dimension has been envisaged by seismicity (Hurst, 1998), geochemistry (Christenson et al., 2010) and hyperspectral imaging (C. A. Miller et al., 2020).

We first perform a background simulation to establish the baseline condition prior to unrest at Ruapehu by injecting hydrothermal fluids (a mix of H_2O and CO_2) at the bottom of the HTS (0 < r < 50 m) over a time span of 3000 years. We then use the resulting distribution of pressure, temperature and gas saturation as the initial condition at t=0 for the subsequent simulations of five unrest scenarios from anomalous injections each lasting for a period of one year (see Table 1 for fluid fluxes). We prescribe atmospheric boundary conditions along the ground surface (P = 0.101325 MPa, T = 10°C, p_{CO2} = 39 Pa), impermeable and adiabatic boundary conditions at the sides, and a basal heat flux of 0.086 W/m^2 (Stern et al., 1987) and impermeability at the base of the model, except for the points of fluid injection.

During multi-phase flow, gas pressures might differ from liquid pressures due to interfacial curvature and capillary forces, where the pressure difference between gas and liquid phases is equal to the capillary pressure (Currenti et al., 2017). For HTU simulations, we define relative permeability and capillary pressure as function of liquid saturation (S_l) following Todesco et al. (2010). We calculate relative permeability $\kappa_{r\beta}$ for phase β = l,g using the Corey function (Brooks (1964); Pruess et al. (1999) and references within):

$$k_{rl} = S_e^4 \quad and \quad k_{rg} = (1 - S_e)^2(1 - S_e^2), \tag{15}$$

with the effective saturation $S_e = (S_l - S_{lr})/(1 - S_{lr} - S_{gr})$, the residual liquid saturation S_{lr} = 0.33 and the residual gas saturation S_{gr} of 0.05 (Todesco et al., 2010; Coco, Currenti, et al., 2016). Capillary pressure is calculated as a linear function of S_l for S $> S_{lr}$, while capillary pressure is set to 0.01 MPa for $S_l < S_{lr}$ (Todesco et al., 2010).

For HTU simulations, we test three different and distinct unrest scenarios (unrest I-III) using a set of injection rates given the absence of accurate observations. Scenario I represents the lowest injection rate while scenario III representing the highest (Tab. 1). Total injection rates are calculated from heat output for background and unrest activity given by Giggenbach and Glover (1975) using a fluid enthalpy of 3000 kJ/kg (Hurst et al., 1991). Injection rates for H_2O and CO_2 are derived from total injection rates using molar ratios of 0.04 and 0.06 for background and unrest simulations, respectively, while higher molar ratios are common during periods of unrest (e.g., Todesco et al., 2010; Rinaldi et al., 2011). Molar ratios for the hydrothermal fluids are chosen in accordance with CO_2 field observations at Ruapehu (see section S5). While the CO_2 flux from unrest I is below the lower bound of recent emission records for unrest II it represents the upper bound. Note that the CO_2 flux for unrest III exceeds recent records (see Fig. S3). However, by including such a flux allows us to study the detectability of geophysical anoma-

Table 1. List of injection rates for HTU simulations. Total fluxes are calculated from heat outputs of Ruapehu's crater lake using a fluid enthalpy of $3{\cdot}10^6$ J/kg (Hurst et al., 1991). Heat outputs range between 200 MW for quiescence and 1000 MW during unrest (Giggenbach & Glover, 1975). Injection rates for H_2O and CO_2 are derived from total fluxes using the fluids' molar ratios.

	Total flux (kg/s)	H_2O (kg/s)	CO_2 (kg/s)	Molar ratio	Heat output (MW)
Background	50	45.5	4.5	0.04	150
Unrest I	70	61	9	0.06	210
Unrest II	200	175	25	0.06	600
Unrest III	330	288	42	0.06	990

lies from slightly higher CO_2 injection rates than recently observed, and identify whether certain anomalies become exclusively detectable at highest injection rates (unrest III).

Resultant deformation, gravity changes and self-potential anomalies are solved using the finite-difference method presented by Coco and Russo (2013) using the coordinate transformation method (Coco et al., 2014). The hydrothermal model dimension is extended radially and vertically for the electro-mechanical HTU simulations as shown in Figure 1c. Boundary conditions for displacement, gravity changes and SP simulations are set to zero at infinity, with an additional free-stress boundary conditions along the ground surface for deformation processes.

3.3.3 Parameterization

We parameterize our models with best-estimate or known values of subsurface conditions at Ruapehu as reported in Table 2. For model domains z > 0 km (edifice, HTS and TZ), we choose rock properties according to Ruapehu's andesitic deposits (Mordensky et al., 2018; Heap, Kushnir, et al., 2020). The HTS is represented by an altered, porous, permeable and water-saturated andesite, whereas the edifice is a stiff, dense, less permeable and less porous andesite. Hydraulic and electric rock properties for the TZ fall between values of the HTS and the edifice. Mechanical and thermal properties (e.g. E, λ) for the HTS, TZ and edifice are assigned in accordance with their porosity and water-saturation.

Thermal properties for the crust are chosen to match a greywacke composition (Mielke et al., 2016), while mechanical parameters such as the rock density (ρ_c) and the dynamic Young's modulus (E_d) are derived from 2D seismic P-wave velocities (Rowlands et al., 2005) using the Brocher (2005) relationships (Eq. S3-4) and a Poisson's ratio of 0.25 (Fig. S2). We convert E_d to static modulus (E_s) using a conversion of $E_s = 0.5{*}E_d$ (e.g., Cheng & Johnston, 1981; Gudmundsson, 1983). We fit crustal density and static Young's modulus (E_c) by a third-order polynomial to obtain a continuous function of depth (z).

$$\rho_c(z) = 0.0018z^3 - 0.3482z^2 - 22.622z + 2542.3 \tag{16}$$
$$E_c(z) = 0.001z^3 + 0.0238z^2 - 0.9019z + 31.153 \tag{17}$$

We set the Biot-Willis coefficient equivalent to the domains rock porosity. In the absence of precise data, we vary α_{BW} in the parameter study (see below) between the rock porosity and 1 for soft materials according to Wang (2000). The electric conductivities of the sub-domains HTS, TZ and edifice are taken from magnetotelluric studies by Ingham et al. (2009) and Jones et al. (2008). In the absence of direct measurements of C_{SP} for Ruapehu, we derive C_{SP} after Revil and Pezard (1998) (Eq. S4) with the fluid conductivity being calculated according to Byrdina et al. (2018) using Ruapehu's crater lake chemistry (see section S4).

We test the influence of selected parameters on modelled unrest anomalies by exploring plausible value ranges of parameters for which either only sparse or no data exist for Ruapehu. For all unrest simulations we investigate the effect of α_{BW} (α_{BW} x 2, x 4) and C_{SP} ($\pm\ 10^{-8}$–$\pm\ 10^{-10}$ V/Pa) on geophysical anomalies individually by varying these parameters in all sub-domains above z = 1.5 km. Additionally, we test different reservoir volumes (8.9-35.7 km^3, Tab. S1) with the reservoir strengths (VxΔP) being equivalent across all volumes tested and source density changes ($\Delta\rho_m$ = 10-300 kg/m^3) for MU simulations.

4 Results

Here we present the results of the unrest simulations. We report the solutions for the temporal evolution of unrest observables on Ruapehu's summit plateau with coordinates r = 500 m and z = 2640 m. We choose the summit plateau due to its flat topography and the opportunity to capture near-field effects from unrest whilst also accounting for operational safety (V. Miller et al., 2003).

4.1 Magmatic unrest simulations

4.1.1 Magmatic unrest anomalies

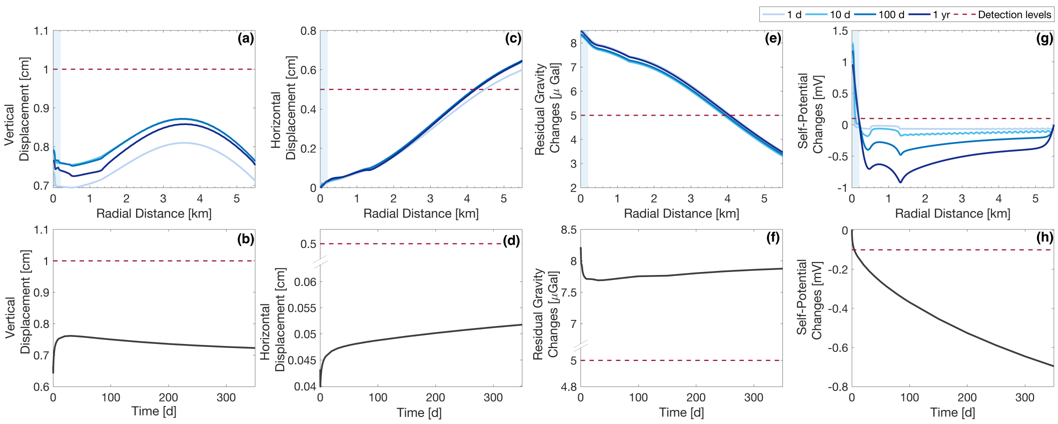

Figure 2. Simulated magmatic unrest anomalies along the ground surface (a,c,e,g) for 1, 10, 100 days and 1 year after source pressurization. Blue shading marks the lateral extend of Ruapehu's crater lake. Lower panels show the temporal evolutions of vertical displacement (b), horizontal displacement (d), residual gravity changes (f) and self-potential anomalies (h) at the plateau (r = 500 m, z = 2640 m).The detection levels are shown by red dashed lines.

Figure 2 shows geophysical anomalies for the reference parameterization of simulated MU. Along the ground surface, we find peak vertical displacements at a distance of 3.5 km from the symmetry axis, with a maximum uplift of 0.87 cm attained 100 days after source pressurization. A localised maximum occurs above the HTS (at r < 50 m) at the bottom of the crater lake with values 0.9 times the maximum amplitude (Fig. 2a). Horizontal displacements peak at a distance of $\sim$ 6.75 km from the deformation centre with amplitudes of $\sim$0.70 cm (see Fig. S9a). Residual gravity changes are at their maximum above the HTS (8.5 μGal at t = 1 d, Fig. 2e) with a linear decrease in signal magnitude with distance from the HTS. Concurrent self-potential anomalies peak above the

Table 2. Model input parameters for reference simulations. Abbreviations: HTS − hydrothermal system, TZ − transition zone, e − edifice, c − crust, f − fluid, MZ − mush zone, m − magma, SP − Self-potential.

Parameter	Value	Reference
E − Young's modulus (GPa)	depth-dependent $-\mathrm{E}_c$ 10 − E_{HTS} 20 − E_{TZ} 30 − E_e	Brocher (2005) Mordensky et al. (2018); Heap, Villeneuve, et al. (2020); Heap, Kushnir, et al. (2020)
ν − Poisson's ratio (/)	0.25 − ν_c 0.3 − ν_{HTS} 0.23 − ν_{TZ} 0.17 − ν_e	Mordensky et al. (2018); Heap, Villeneuve, et al. (2020); Heap, Kushnir, et al. (2020)
ρ − rock density (kg/m^3)	depth-dependent − ρ_e 2200 − ρ_{HTS} 2400 − ρ_{TZ} 2500 − ρ_e	Brocher (2005) Gudmundsson (2011); Mielke et al. (2016); Heap, Kushnir, et al. (2020)
α_{BW} - Biot-Willis (/)	0.2 − $\alpha_{BW_{HTS}}$ 0.15 − $\alpha_{BW_{TZ}}$ 0.1 − α_{BW_e}	Wang (2000)
σ − electrical conductivity (S/m)	1− σ_{HTS} 0.3 − σ_{TZ} 0.1 − σ_e 9.5 − σ_f	Jones et al. (2008); Ingham et al. (2009) equation S5 (Byrdina et al., 2018)
C_{SP} - SP coupling coefficient (V/Pa)	10^{-9}	calculated from Revil and Pezard (1998) (S4)
α_T − thermal expansion coefficient (1/K)	$3.5 \cdot 10^{-4}$ − α_T	Hurst and Dibble (1981)
c − heat capacity (J/K)	910 − c_e 1025 − c_{HTS} 780 − c_{TZ} 730 − c_e	Mielke et al. (2016); Heap, Kushnir, et al. (2020)
λ − thermal conductivity (W/m K)	2.2 − λ_c 1.36 − λ_{HTS} 1.15 − λ_{TZ} 1.23 − λ_e	Mielke et al. (2016); Heap, Kushnir, et al. (2020)
W − crustal heat flux (W/m^2)	0.086	Stern et al. (1987)
H − fluid enthalpy (MJ/kg)	3	Hurst et al. (1991)
T_{MZ} − MZ temperature [K]	1303.15	G. N. Kilgour et al. (2014)
κ − permeability (m^2)	10^{-12} − κ_{HTS} 10^{-14} − κ_{TZ} 10^{-16} − κ_e	e.g. Hurst et al. (1991); Christenson (2000); Heap et al. (2017); Mordensky et al. (2018)
ϕ − porosity (/)	0.2 − ϕ_{HTS} 0.15 − ϕ_{TZ} 0.1 − ϕ_e	Heap et al. (2017); Mordensky et al. (2018)
ρ_f − fluid density (kg/m^3)	1020	Christenson (1994)
η_f − fluid viscosity (Pa s)	10^{-3}	Fetter (2013); Turcotte and Schubert (2002)
χ_f − fluid compressibility (1/Pa)	$4 \cdot 10^{-10}$	
χ_m − magma compressibility (1/Pa)	$1.25 \cdot 10^{-10}$	Gudmundsson (1987)
b_{HTS} − HTS bottom (m)	1500	Christenson et al. (2010);
t_{HTS} − HTS top (m)	2640	C. A. Miller et al. (2020); Hurst (1998)
r_{HTS} − radius the HTS (m)	50	
r_{MZ} −radius of the MZ (km)	0.78	see S1
b_{MZ} − MZ bottom (km)	-2	Rowlands et al. (2005); Ingham et al. (2009); G. N. Kilgour et al. (2013); Jolly et al. (2010)
t_{MZ} − MZ top (km)	-9	
ΔP − source pressure change (MPa)	10	
$\Delta\rho_m$ − source density change (kg/m^3)	10	
V − source volumes (km^3)	17.9	calculated (see section S2)

HTS ($SP_{max} \sim 1.3$ mV at t = 10 days) with anomalies rapidly falling off to negative values at distances r< 400m from the HTS.

The temporal evolution of the unrest observables at the plateau (r = 500 m and z = 2640 m) are illustrated in Figure 2 (lower panels). We find a maximum amplitude change of 0.10 cm for vertical displacement (w) in the edifice within the first 30 days after source pressurization, with peak magnitudes of 0.76 cm at t = 30 days. Horizontal displacement (u) shows an initial minimum of 0.04 cm followed by a continuous increase in magnitude with time. After 350 days (referred to as 1 year hereafter) maximal u at the plateau is 0.07 times smaller than the peak magnitude ($u \sim 0.7$ cm) at r = 6.75 km (Fig.2d and S9b). Residual gravity changes (δg_r) decrease rapidly within the first 30 days with a maximum change of 0.5 μGal. SP anomalies decrease linearly with time showing an absolute amplitude change of 0.7 mV.

4.1.2 Parameter exploration

For large reservoir volumes (Fig. 3 left panels) > 7.2 km^3/MPa, we observe magnitudes of 1.3, 1.4 and 2.1 times the initial reference values for vertical displacement, horizontal displacement and residual gravity changes, respectively. SP anomalies remain broadly unchanged for the explored reservoir strength variations.

An increase in Biot-Willis coefficient (α_{BW}, Fig. 3 right panels) reduces vertical displacements relative to reference values throughout time, while horizontal displacements are reduced for t < 75 days but increased thereafter. Residual gravity changes and SP anomalies are amplified with respect to the initial reference values for the highest α_{BW} tested (α_{BW} x 4).

Figure 4a shows the impact of varying the source density change ($\Delta\rho_m$) on residual gravity changes (δg_r). We find a correlation between peak δg_r and $\Delta\rho_m$, with greatest δg_r of 35 times reference amplitudes for $\Delta\rho_m = 300$ kg/m^3. Polarity of δg_r corresponds to $\Delta\rho_m$ polarities.

The influence of the streaming-potential coupling coefficient (C_{SP}) on SP anomalies is shown in Figure 4b. For the highest C_{SP} tested (10^{-8} V/Pa), SP magnitudes are amplified up to 10 times the initial reference value, while SP amplitudes for $\pm C_{SP} = 10^{-10}$ V/Pa show negligible changes. SP time series for negative and positive C_{SP} polarities are inverted.

4.2 Hydrothermal unrest simulations

4.2.1 Hydrothermal injection

Panels a, e and i in Figure 5 depict the initial pore pressure, temperature and gas saturation distributions after background injection over 3000 years. We find peak pore pressures around the injection area (r < 50 m, z = 1.5 km) whereas the far-field pore pressure distribution mirrors the topography. Temperature and gas saturation are elevated around the HTS, with highest temperatures of ~300°C at the bottom of the HTS. Maximal gas saturation are simulated below the crater lake (z ~ 2440 m, r < 200 m).

Relative to background distributions, variations in pore pressure (Δp_f), temperature (ΔT) and gas saturation (ΔS) correlate with anomalous fluid fluxes (Fig. 5). We observe maximum (Δp_f) of 9 MPa, ΔT of 60°C and ΔS of 0.6 for unrest III after 1 year of anomalous injection (Fig. 5 panels d, h and l). For unrest I, concurrent amplitudes changes of (Δp_f), ΔT and ΔS are between 0.1−0.18 times maximum amplitudes of unrest III. Variations in pore pressure, temperature and gas saturation are confined to the HTS and its proximity, whereas the far-field is broadly undisturbed. For increasing injection rates, the gas plume propagates further towards the surface and additionally dispersing into the TZ at z = 1.5 km.

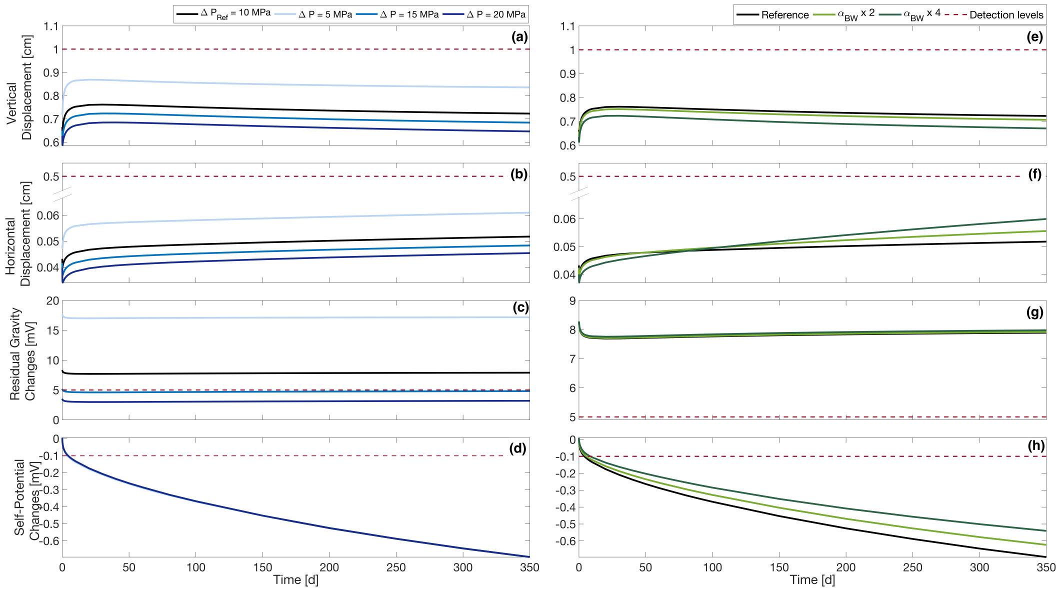

Figure 3. Influence of varying source volume(V (a-d)) and Biot-Willis coefficient (α_{BW} (e-h)) on time series of simulated MU anomalies at the plateau (r = 500 m, z = 2640 m). Biot-Willis coefficient is varied in all poroelastic domains simultaneously. The red dashed lines mark the detection limits, with ground displacements remaining undetectable, and residual gravity and self-potential changes above detection limits.

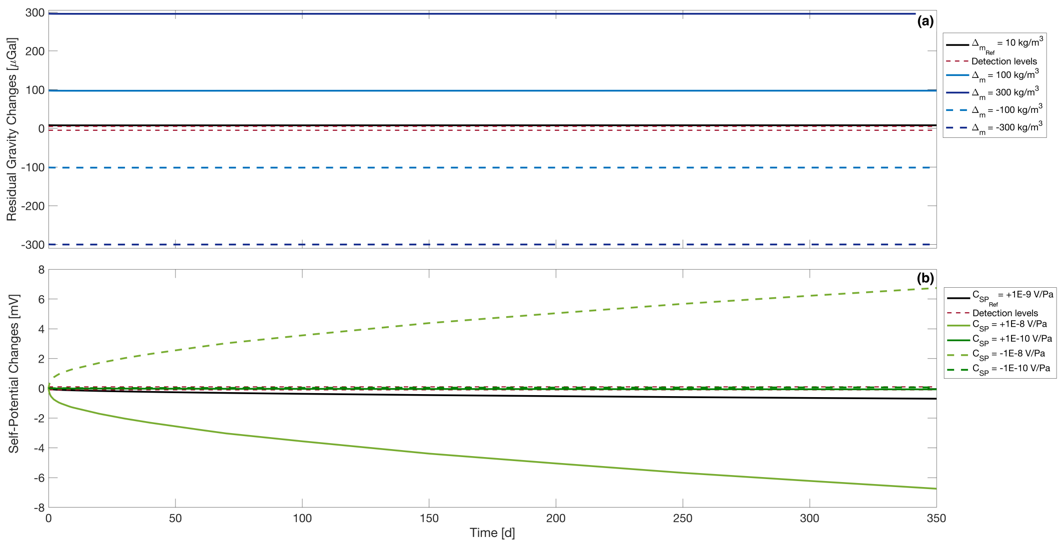

Figure 4. Effect of varying source density change ($\Delta\rho_m$) and streaming-potential coupling coefficient (C_{SP}) on residual gravity changes (ΔG, a) and self-potential (SP, b) anomalies at the plateau, respectively. Most δg_r and SP magnitudes are above detection levels (red dashed lines).

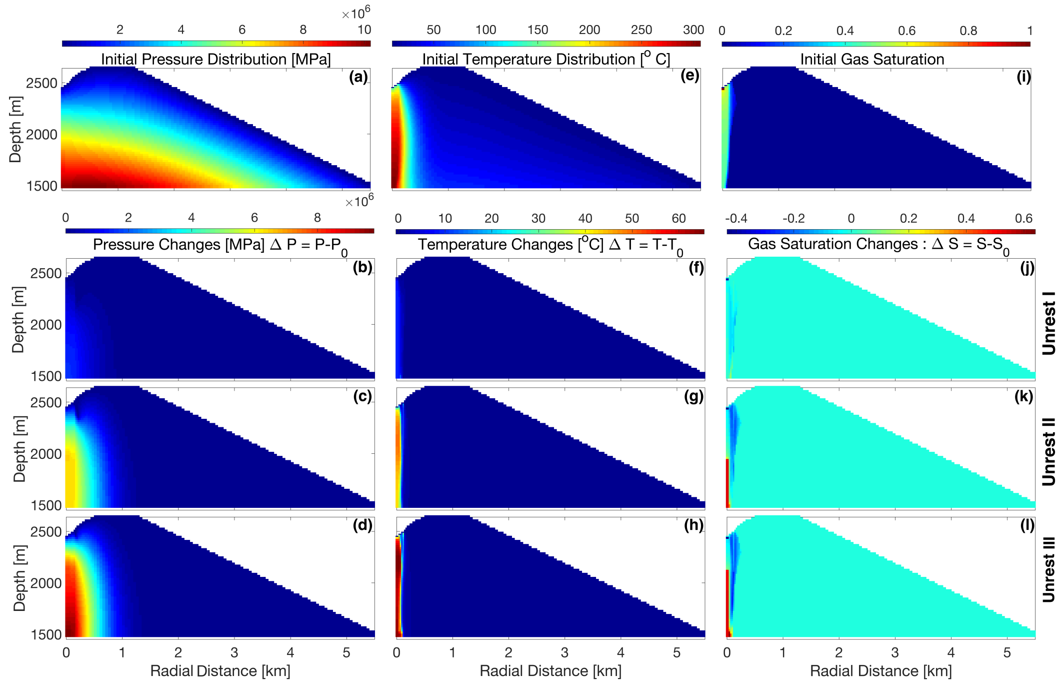

Figure 5. Simulation of hydrothermal fluid flow. Upper panels show the background distribution of pore pressure (a), temperature (e) and gas saturation (i) after 3000 years of continuous injection of 45 kg/s H_2O and 5 kg/s CO_2 at a temperature of 350°C. Initial conditions are used for three unrest simulations (I-III, lower panels). Variations in pore pressure (b-d), temperature (f-h) and gas saturation (j-l) with respect to the background simulation are illustrated for 1 year of anomalous injection. Unrest III represents the highest injection rate (use table 1 for fluid fluxes). Note different colour scales for initial and unrest simulations.

4.2.2 Hydrothermal unrest anomalies

Figure 6 (panels a-h) shows the results of simulated HTU anomalies along the ground surface at different times since anomalous injections. We find peak (positive/negative) anomalies except for horizontal displacements (maximum u at r $>$ 50 m) directly above the HTS with magnitudes falling off rapidly with distance to the HTS.

After 1 year of anomalous injection, maximum vertical uplift of $\sim$ 3 cm and horizontal displacement (u) of $\sim$ 1.3 cm is observed for unrest III, while unrest I induces magnitudes 14% and 9% of maximum w and u, respectively. Residual gravity changes are of negative polarity with minimal values above the HTS ranging between -83 μGal (unrest III) and -18 μGal (unrest I) at t = 350 days and t = 100 days, respectively. Self-potential anomalies (Fig.6, panels d and h) peak above the HTS with the maximum of 6.5 mV (1 year) corresponding to the highest injection rate, while SP anomalies resulting from unrest I are only of 0.63 mV.

Time series of simulated HTU anomalies at the plateau are illustrated in Figure 6 (panels i-l). Vertical and horizontal displacements exhibit similar temporal evaluations with increasing magnitude with time and a maximum of $\sim$ 0.86 cm for w and u for unrest III at t = 350 days. Residual gravity changes decrease monotonically with time for unrest I , whereas δg_r for unrest $\geq$ II show time-delayed minima at 100 (δg_r = - 7.8 μGal greatest minimum) and 200 days for unrest III and II, respectively. SP time series fluctuates throughout time with an overall increase of SP amplitudes for unrest $\geq$ II with time, while SP anomalies for unrest I remain broadly unchanged. Maximum SP amplitudes of 2.6 mV are observed for unrest III, which is 8.5 times the SP magnitude of unrest I.

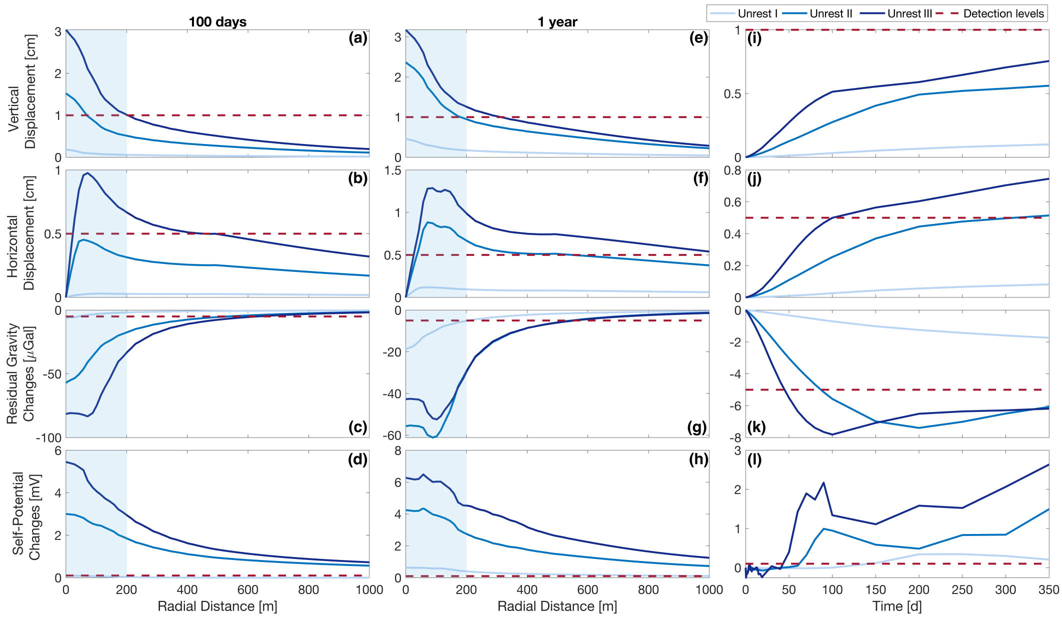

Figure 6. Simulated hydrothermal unrest anomalies along the surface (a-h) for 100 days and 1 year of anomalous injection. Three injection rates (unrest I-III) are tested with unrest III representing the highest fluid flux. Blue shading marks the extent of Ruapehu's crater lake. Time series at the plateau (r = 500 m, z = 2640 m) are shown for (i) vertical displacement, (j) horizontal displacement, (k) residual gravity changes and (l) self-potential anomalies. Results for t=10 days are not shown as all signals are below detection levels (dashed red lines; see also Fig. S10).

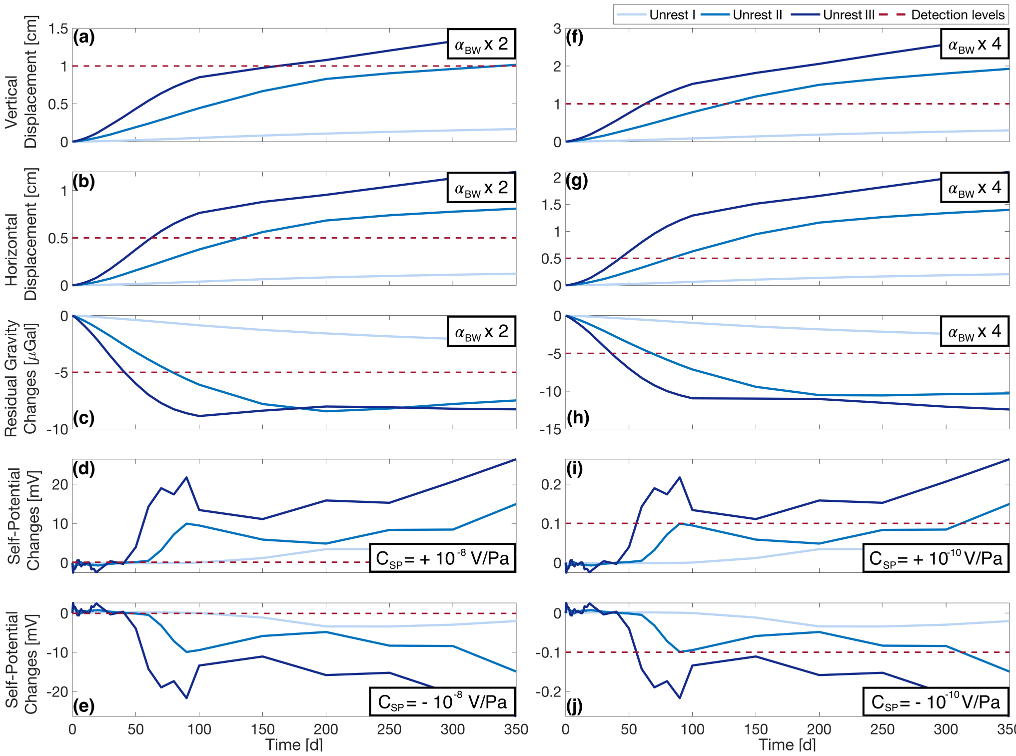

Figure 7. Results of parameter exploration on simulated HTU anomalies at the plateau (r = 500 m, z = 2640 m) for unrest I-III. Upper panels (a-c,f-h) show the influence of Biot-Willis coefficient (α_{BW}) on ground displacements and residual gravity changes. The effect of the streaming-potential coupling coefficient (C_{SP}) on SP anomalies with time is shown in the lower panels (d-e,i-j). α_{BW} and C_{SP} are studied individually, but varied in all poroelastic domains simultaneously. The detection limits of signals are shown by red dashed lines. Most signals exceed detection levels.

4.2.3 Parameter exploration

The upper panels in Figure 7 show the influence of Biot-Willis coefficient (α_{BW}) on temporal ground displacements at the plateau. Displacements correlate positively with α_{BW}. For the largest values tested (α_{BW} x 4), we obtain vertical displacements up to 3.5 times (unrest III) higher than the maximum reference amplitude, with similar changes in magnitude for horizontal displacements. Residual gravity changes decrease with increasing α_{BW} with minimum values of -13 μGal for unrest III, which is 1.6 times the reference minimum.

Figure 7 (lower panels) shows the effect of the streaming-potential coupling coefficient (C_{SP}) on temporal SP anomalies. While C_{SP} values strongly control the SP amplitudes and polarities, the temporal evolution mirrors the reference time series (Fig. 6l) for positive C_{SP}, but is inverted for negative C_{SP} polarities. We find that SP anomalies vary up to a factor of 10 (unrest III) smaller or greater than that of the reference SP amplitude for negative or positive C_{SP}, respectively.

5 Discussion

Our multiphysical modelling approach is the first study investigating multi-parametric anomalies from magmatic and hydrothermal unrest processes at Ruapehu. We have shown that magmatic and hydrothermal perturbations induce markedly different spatio-temporal observables. Simulation results depend strongly on underpinning model assumptions and parameterization which in our study are constrained by geophysical, geological and petrological data.

5.1 Magmatic unrest simulation

5.1.1 Magmatic unrest anomalies

While spatial ground displacement patterns from magmatic unrest simulations are broadly similar to predictions from time-independent elastic half-space solutions for a prolate magma reservoir at Ruapehu (V. Miller et al., 2003), we note several key differences: i) a non-linear evolution of ground displacements due to poroelasticity in the edifice and crustal viscoelasticity (see Fig. 2 and S4), ii) poroelasticity in the HTS and TZ reduces the magnitude of vertical displacement w for r < 200 m and iii) reduced (by up to 50%) magnitudes of ground displacements in our study. The latter corroborates results reported in Males and Gottsmann (2021) where subsurface heterogeneity and volcano prominence control the stress and strain partitioning and hence the displacement magnitudes. Additionally, the displacement magnitude is controlled, as expected, by elastic parameters, source pressure (ΔP) and the location and dimension of the magmatic reservoir (e.g., Hickey et al., 2013).

Subsurface displacements influence residual gravity changes through the gravity contributions from host rock compression and shifting density boundaries (Eq. 11). However, these contributions are of minor importance in our study as δg_r is predominantly governed by source density changes (see Fig. S5), corroborating findings reported in Gottsmann, Biggs, et al. (2020). As $\Delta\rho_m$ remain constant throughout time, the temporal evolution of δg_r is opposite to the temporal evolution of w due to the free-air effect. In terms of spatial patterns, we find an agreement of δg_r along the ground surface between our study and findings in Currenti (2014), with peak amplitudes directly above the HTS. The temporal evolution of δg_r is similar to that of the vertical displacement governed by poroelastic responses of the edifice and viscoelastic processes in the crust. Visco-poroelastic processes appear to dominate ground deformation at the beginning of the perturbation (see Fig. 2) with ground subsidence following initial uplift. This compares to subsidence only in simulations accounting for poroelastic effects (see Fig. S4). However, given the resolution limit of geodetic observations neither process is detectable.

Self-potential anomalies from strain-induced fluid flow peak above the HTS, where pore pressure variations are at their largest (Eq. 13). We find an absolute SP change of 0.7 mV after 1 year of magmatic perturbation. The continuous decrease in SP magnitude with time indicates a drop in pore pressure as C_{SP} and pore pressure are positively correlated in this study, as opposed to the inverse relationship for non-acidic waters described elsewhere (Revil, Saracco, & Labazuy, 2003; Rizzo et al., 2004).

5.1.2 Parameter exploration

The parametric study revealed minor variations in ground displacement magnitudes with changing reservoir volumes and Biot-Willis coefficients (α_{BW}). Since reservoir strength is kept constant in all simulations, resultant ground deformations are controlled by visco-poroelastic responses of the surrounding media to induced pressure perturbations compared to reference solutions. In a one-way coupling approach ground displacement correlates with pore pressure changes and α_{BW} (Currenti & Williams, 2014; Raziperchikolaee et al., 2020). However, in our two-way coupling approach where Δp_f affects stresses and strains and vice versa, the effect of α_{BW} on radial displacements in particular is more complex. Ground displacements are generally controlled by stress and pore pressure changes in response to subsurface heterogeneities (see Strehlow et al. (2015); Hickey and Gottsmann (2014)). Residual gravity changes are strongly influenced by changes in source density and pressure ($\Delta\rho_m$ and V, respectively). We show that $\Delta\rho_m$ and δg_r correlate in terms of magnitude. In our MU models, δg_r are primarily governed by the increase in source density as a result of the injection of new magma, a common assumption behind episodes of unrest at Ruapehu (G. N. Kilgour et al., 2013; Nakagawa et al., 1999). . Source density changes of 10 kg/m^3 in greater reservoir volumes results in larger δg_r values compared to the reference simulation. The dependency of δg_r on α_{BW} is negligible across the range of tested values, as the effect of α_{BW} on displacements of density boundaries is much smaller than the effect of source density changes (see section 5.1.1).

Similar to findings in Arens et al. (2020), our study finds that SP anomalies are governed by electrokinetic processes arising from poroelastic responses to subsurface perturbations and are hence primarily controlled by α_{BW}. Furthermore, we show that SP magnitudes are markedly controlled by C_{SP} matching results reported by Arens et al. (2020), where C_{SP} is categorised as an influential parameter.

5.2 Hydrothermal unrest simulation

5.2.1 Hydrothermal injection

The injection of hydrothermal fluids disturbs the physicochemical conditions in the subsurface and manifests as variations in pore pressure, temperature and gas saturation in the subsurface (Fig.5). Comparing our results with findings reported in Christenson et al. (2010) we note differences in model parameterization (e.g., injection rates, parameters), model setup (e.g., flat surface, initial conditions) and HTS volume compared to our study. Although simulated background gas saturation and temperature distributions in our study broadly resemble the background conditions of Ruapehu considered in Christenson et al. (2010), temporal changes in the gas and temperature distribution in our study are predicted over a much larger space. This might result from a wider injection area and a longer-lasting injection period compared to the study of Christenson et al. (2010). Unlike the linear pore pressure evolution in other studies (e.g., Christenson et al., 2010; Stissi et al., 2021), we simulate elevated initial pore pressures around the HTS and its proximity after protracted background injection. As a result pore pressures reach $\sim$10 MPa around the injection area and are similar to the pore pressure parameterization in Coco, Gottsmann, et al. (2016). The overall pattern of pore pressure distribution mirrors topography, indicating that topographic effects must be taken into account when investigating fluid flow in a volcanic edifice (Fig. 5a).

Transient variations of pore pressure, temperature and gas saturation caused by anomalous injection are confined to the injection area (HTS) and its proximity as observed by Coco, Currenti, et al. (2016). Similar to findings reported in Christenson et al. (2010), pressure and temperature pulses (relative to the background) propagate towards the crater lake bottom over time (Fig. 5, S7 and S8). Note though, that in contrast to the simulated intrusion of gases into the crater lake in Christenson et al. (2010), in our study a deep-seated single-phase gas plume develops in the HTS (see Figs. 5 and S6). Furthermore, the drop in ΔS below the crater (Fig. 5 panels j-l, r<200m) indicates that liquid H_2O enters previously gas-enriched areas as it migrates quickly through permeable domains (e.g., Todesco et al., 2010), such as the HTS and TZ. The positive correlations between injection rates and magnitudes of Δp_f, ΔT and ΔS match results reported in Coco, Gottsmann, et al. (2016).

5.2.2 Hydrothermal unrest anomalies

We find similarities in the spatial displacement patterns from HTU simulations to findings reported in Stissi et al. (2021) and Currenti et al. (2017). Here, highest vertical displacements correlate with largest pore pressure and temperature variations (Fig. 5). As peak (Δp_f) and ΔT values are encountered around the HTS, vertical displacements fall off rapidly with distance from the HTS. We find that ground displacements increase with both injection rate and time due to the thermo-poroelastic response caused by protracted pore pressure and temperature variations. That is to say that ground displacements evolve in unison with the severity of hydrothermal unrest matching findings in Coco, Gottsmann, et al. (2016).

In contrast to ground displacements, magnitudes of residual gravity changes correlate negatively with fluid fluxes. The spatio-temporal behaviour of δg_r is controlled by fluid density variations (e.g., Todesco & Berrino, 2005; Todesco, 2009; Coco, Currenti, et al., 2016). That is to say, in areas where H_2O replaces gases (e.g., in the TZ; increase in $\Delta\rho_f$) positive δg_r are expected, while negative δg_r arise where gas-rich fluids ascend (e.g., in the HTS; drop in $\Delta\rho_f$). Subsurface heterogeneities strongly govern the distribution of H_2O and CO_2 (Todesco et al., 2010). For instance, the permeable HTS favours the upwards migration of H_2O and CO_2 due to influx of new fluids at its base, which might prompt the discharge of H_2O at the surface causing an overall decrease in $\Delta\rho_f$ and δg_r. This behaviour could explain the negative δg_r values directly above the HTS.

Spatio-temporal H_2O and CO_2 fluctuations govern (Δp_f) and hence electrokinetic processes. SP magnitudes correlate with (Δp_f) for the strongest hydrothermal unrest, with an overall increase in SP amplitude over time for protracted hydrothermal unrest (> 200 days). We find that the spatial SP pattern matches observations at other volcanoes (volcano-electric effect after Revil, Saracco, and Labazuy (2003)) with peak SP anomalies directly above zones of hydrothermal upflow (Zlotnicki & Nishida, 2003).

5.2.3 Parameter exploration

We show that the Biot-Willis coefficient influences geodetic anomalies from hydrothermal perturbations. Ground displacements are governed by the poroelastic response of the one-way coupling approach (Eq. 3.2.1) and are hence controlled by (Δp_f) and α_{BW}. That is to say, that uplift correlates with Δp_f and α_{BW} (see also Raziperchikolaee et al. (2020)). The choice of poroelastic coupling (one-way vs two-way) could explain the different effect of α_{BW} on displacements between HTU and MU simulations. The influence of α_{BW} on δg_r is predominantly caused by the gravity contributions from the free-air effect and hence w; i.e., δg_r magnitudes decrease for increasing α_{BW} (and w). SP anomalies are not governed by α_{BW} in HTU simulations due to the one-way coupling approach. Like in our MU parametric simulations, SP magnitudes from hydrothermal perturbation correlate with the key parameter C_{SP}.

5.3 Implications for geophysical unrest monitoring at Ruapehu

While changes in ground elevation are routinely monitored at Ruapehu, monitoring of SP and gravity changes is absent. It is interesting to note that prior to the most recent magmatic eruption at Ruapehu in 2007, no ground displacements were observed (Mordret et al., 2010). To explain this and to identify geophysical anomalies indicative of magmatic or hydrothermal unrest, we compare the simulated magnitudes of ground displacements as well as SP and gravity changes with detection levels of conventional surveying techniques. Our analysis is focused on the near-field of the crater lake at the plateau (r = 500 m, z = 2640 m) where instrumentation could be deployed and maintained.

Ground displacements from MU simulations remain below the detectability limits of 1 cm vertically and 0.5 cm horizontally by GNSS surveys (Mordret et al., 2010) on the plateau. However, horizontal displacements become detectable at a distance of 6.75 km from the HTS (see Fig. S9). Our parametric investigations from MU simulations show that ground displacements at the plateau remain below detection levels even at the largest magmatic perturbation explored in this study. The detectability of ground displacements from HTU simulations is complex and differs for horizontal and vertical displacement. Although w displacements in reference simulations are below conventional detection limits, u displacements are detectable for unrest $\geq$ II. For unrest III conditions, u exceed detection limits after a much shorter period of time (at t $\sim$ 100 days) compared to unrest II (at t = $\sim$ 300 days). As such the geodetic detectability of unrest depends on the magnitude of subsurface perturbations. For the largest Biot-Willis coefficient explored in this study, the peak u displacement becomes detectable after a shorter time compared to the reference simulations (e.g., unrest III at t $\sim$ 50 days vs. unrest II at t = $\sim$ 90 days). Additionally, w during unrest $\geq$ II exceeds detection limits for all α_{BW} values tested. The absence of pre-eruptive displacement anomalies in the most recent phreatic eruption might be explained by anomalous hydrothermal injection at rates similar to conditions simulated in unrest I.

Residual gravity changes from MU reference and most parametric simulations are above detection levels of ± 5 μGal (Battaglia et al., 2008), but their temporal variations remain undetectable. For HTU reference simulations, injection rates $\geq$ unrest II induce measurable δg_r after >40 days of anomalous injection, while δg_r from fluid fluxes I remain undetectable throughout. Higher α_{BW} values result in higher δg_r values and favour their detectability.

The self-potential anomaly from protracted unrest reaches an absolute change of 0.7 mV (MU simulations), while SP anomalies range between <0.5 to a maximum of $\sim$ 2.5 mV for unrest I and III in the HTU simulations, respectively. SP magnitudes from subsurface perturbations fall within the detectability levels of standard field observations (0.1 mV; Grobbe and Barde-Cabusson (2019); Revil and Jardani (2013)). Parametric studies for both unrest scenarios have shown that SP magnitudes increase significantly with increasing the streaming-potential coupling coefficient.

Although some simulations predict ground displacements, gravity changes and perturbations in self-potential above detectability limits, the temporal evolutions of the signals are predicted to be difficult to resolve. However, some combinations of observables are indicative of source processes. For example, a temporal decrease in w displacements and simultaneous increase in u displacements might indicate magma pressurization and the time-dependent visco-poroelastic response of the surrounding media. The temporal evolution of δg_r is similar in both HTU and MU simulations whereby the signal amplitude decreases initially followed by an increase. However, δg_r values are positive in MU simulations and negative in HTU simulations. Fluid density distribution from HTU simulations depends on the spatio-temporal distribution of gas and liquid in the subsurface and fluctuates as a result of fluid injections and redistribution. Therefore the change in magnitude of δg_r with time is more pronounced in HTU simulations compared to MU simulations (see Fig. 2 and 6). Self-potential anomalies decrease in MU simulations with time but increase in HTU simulations (see Fig. 2 and 6).

We identify distinct sets of detectable geophysical anomalies at Ruapehu's plateau which could be used to interrogate the nature of volcanic unrest. We find that density changes in the crustal mush zone and electrokinetic processes from strain-induced fluid flow in the volcanic edifice (z > 1.5 km) induce measurable gravitational and electrical potential field anomalies at the plateau and hence are indicative of magmatic unrest. Horizontal displacements in the far-field might act as additional indicators of source pressurization (MU simulations), but ground displacements in the proximity of the HTS are not detectable. Protracted hydrothermal unrest is identifiable by SP anomalies for all HTU simulations and ground displacements for unrest $\geq$ II. In addition, residual gravity changes become a distinctive fingerprint of HTU for CO_2 fluxes matching those during the 2007 unrest (i.e., unrest II). This implies that protracted hydrothermal unrest at the higher end of CO_2 fluxes explored in our models (unrest III) yields detectable residual gravity changes. We therefore recommend the implementation of continuous gravity and self-potential monitoring at Ruapehu, which in combination with existing monitoring techniques (e.g. seismicity, fluid chemistry) at Ruapehu could significantly improve interpretations of source processes during unrest periods. The summit plateau would be suitable to safely locate monitoring instrumentation (V. Miller et al., 2003); based on our findings a combination of the three geophysical signals from either magmatic or hydrothermal perturbation is detectable. As continuous GNSS sites at Ruapehu are located > 500 m from the HTS (http://www.geonet.org.nz), we suggest the implementation of GNSS sites at the summit plateau to allow for signal detectability (e.g. HTU). Most signals fall off rapidly with distance from the HTS; locating monitoring sites at r

$>$ 500 m drastically reduces signal detectability. At the same time, installing and maintaining monitoring stations closer to the HTS could be challenging due to the steep topography and potential impact of ballistics during eruptions (G. Kilgour et al., 2010; Strehlow et al., 2017).

5.4 Model limitations

We use a simplified model geometry (2D axisymmetrical) to keep simulations computationally cost-efficient, but sufficiently complex to gain first-order insights into geophysical anomalies caused by magmatic and hydrothermal unrest at Mt. Ruapehu. Both unrest processes are studied in isolation, while in reality magmatic and hydrothermal perturbations might superimpose. Furthermore, we do not account for the interaction of magma with the hydrothermal system. All models presented in this study incorporate subsurface mechanical, electrical and hydraulic heterogeneity and account for a topography representative of the volcano. All of the multi-parametric data sets that helped constrain our models are either 1D or 2D. Should 3D variations of these parameters become available, the models can be adapted to provide 3D solutions.

Inherent model limitations for MU simulations have been described in detail in Arens et al. (2020). Our HTU simulations do not account for super-critical conditions, although there is evidence for pressures and temperatures in hydrothermal systems at active volcanoes exceeding the critical point of water (Reinsch et al., 2017). The thermo-poroelastic coupling approach used in this study is most representative of short-term hydrothermal perturbations (Coco, Gottsmann, et al., 2016) with applications to many volcanoes (e.g., Fournier & Chardot, 2012; Todesco & Berrino, 2005; Currenti & Napoli, 2017). However, it has been shown that a two-way coupling approach is more applicable for temporally protracted perturbations (Neuzil, 2003; Rutqvist et al., 2002), where subsurface strain affects hydraulic rock properties (e.g., κ, ϕ) which in turn govern the flow behaviour and in turn stresses and strains. Similar to studies by e.g., Hutnak et al. (2009); Currenti et al. (2017); Fournier and Chardot (2012); Rinaldi et al. (2011), we neglect the effect of (i) shifting density boundaries and (ii) host rock compression on residual gravity changes. Gravity contributions from (i) and (ii) in our study are 0.2 μGal and -0.4 μGal, respectively, and hence almost cancel one another out. Therefore we deduce fluid density changes from hydrothermal perturbations as the main source of δg_r changes. The inclusion of the aforementioned effects and the two-way coupling approach would be a next step of studying hydrothermal unrest at Ruapehu.

Neither of our simulations account for the temperature dependence of parameters such as permeability (Ikard & Revil, 2014), fluid properties (Arens et al., 2020) or elastic parameters (Head et al., 2021), all of which have an effect on geophysical anomalies modelled in our study; a dedicated analysis is required to assess this influence. Although we neglect thermoelectric processes caused by strong thermal gradients (Corwin & Hoover, 1979; Fitterman & Corwin, 1982) in the HTU simulations, we find that for a maximum temperature change of 0.18 °C (unrest III) at the plateau, the thermoelectric potential (TEP) is $\pm$ 0.3 mV and 0.1 mV using a thermoelectric coupling coefficient of $\pm$ 1.5 mV/°C and $\pm$ 0.5 mV/°C (Revil & Mahardika, 2013; Ikard & Revil, 2014), respectively. The TEP is only 5−15% of the maximum SP amplitude, so we conclude that electrokinetic processes dominate electrical potential field changes.

6 Conclusions

We have utilised multiphysics models to study volcanic unrest and concurrent geophysical anomalies at the active volcano Mt. Ruapehu. Our study was able to discriminate spatio-temporal anomalies that might help identify the nature of unrest (hydrothermal vs magmatic). While gravitational and electrical potential field anomalies are indicative of magmatic processes (e.g., source pressurization and density changes) in the sub-volcanic mush zone, ground displacements (vertical and horizontal) in the proximity of the deformation source remain below detection limits for reference and parametric simulations. However, horizontal displacements become resolvable in the far-field and could provide additional insights into magmatic unrest. In contrast, ground displacements, residual gravity changes and SP anomalies from hydrothermal unrest are detectable in the near-field.

Parameter space testing show the major control of some key model parameters (e.g., α_{BW}, C_{SP}, V) on the detectability of geophysical anomalies. For instance, magnitudes of SP and residual gravity changes correlate with key parameters C_{SP} and Δ_m, respectively. While the superposition of magmatic and hydrothermal perturbations need to be taken into account when interpreting observed precursors, we have identified unique sets of resolvable magnitudes of geophysical anomalies from either subsurface perturbation. We conclude that joint and simultaneously collected multi-parameter time series should provide valuable insights into unrest source mechanisms, especially when corrected for non-volcanic background processes. In order to distinguish between frequent hydrothermal unrest and less-frequent but potentially more violent magmatic unrest at Ruapehu, we propose the implementation of routine self-potential and gravity monitoring to support ongoing monitoring efforts. The findings reported here may have implications for assessing unrest dynamics at other crater lake volcanoes.

Data Availability Statement

No data were created or used for this research.Model scripts are available from http://zenodo.org (doi:10.5281/zenodo.7304472).

Acknowledgments

JG, JH and GK conceived the research project behind this study. FA designed and conducted the simulations with input from JG and AC. FA drafted the initial manuscript, with the final manuscript receiving input from all authors. FA is supported by a NERC GW4+ Doctoral Training Partnership studentship from the Natural Environment Research Council (NERC; NE/L002434/1) and is thankful for the support and additional funding from CASE partner GNS Science and DEVORA. AC acknowledges support from GNCS-INDAM (National Group for Scientific Computing, Italy). GK acknowledges support from the New Zealand Ministry of Business, Innovation and Employment (MBIE) through the Hazards and Risk Management programme (Strategic Science Investment Fund, contract C05X1702). We thank YQ Wong and an anonymous reviewer for their constructive and valuable comments, which helped to improve the manuscript.

References

Arens, F., Gottsmann, J., Strehlow, K., Hickey, J., & Kilgour, G. (2020). Electrokinetic Contributions to Self-Potential Signals From Magmatic Stressing. *Geochemistry, Geophysics, Geosystems*, *21*(12), 1–21. doi: 10.1029/2020GC009388

Battaglia, M., Gottsmann, J., Carbone, D., & Fernández, J. (2008). 4D volcano gravimetry. *Geophysics*, *73*(6). doi: 10.1190/1.2977792

Biot, M. A. (1962). Mechanics of Deformation and Acoustic Propagation in Porous Media. *Journal of Applied Physiscs*, *33*(4), 1482–1498. doi: https://doi.org/10.1063/1.1728759

Bolève, A., Janod, F., Revil, A., Lafon, A., & Fry, J. J. (2011). Localization and quantification of leakages in dams using time-lapse self-potential measurements associated with salt tracer injection. *Journal of Hydrology*, *403*(3-4), 242–252. doi: https://doi.org/10.1016/j.jhydrol.2011.04.008

Bonafede, M. (1991). Hot fluid migration: an efficient source of ground deformation: application to the 1982-1985 crisis at Campi Flegrei-Italy. *Journal of Volcanol-*

ogy and Geothermal Research, *48*(1-2), 187–198. doi: 10.1016/0377-0273(91)90042-X

Bonafede, M., & Mazzanti, M. (1998). Modelling gravity variations consistent with ground deformation in the Campi Flegrei caldera (Italy). *Journal of Volcanology and Geothermal Research*, *81*(1-2), 137–157. doi: 10.1016/S0377-0273(97)00071-1

Brocher, T. M. (2005). Empirical relations between elastic wavespeeds and density in the Earth's crust. *Bulletin of the Seismological Society of America*, *95*(6), 2081–2092. doi: 10.1785/0120050077

Brooks, A. T., R. H. Corey. (1964). Hydraulic properties of porous media. *Colorado State 599 University Hydrology*, *3*, 293–296.

Browning, J., Drymoni, K., & Gudmundsson, A. (2015). Forecasting magma-chamber rupture at Santorini volcano, Greece. *Scientific Reports*, *5*, 1–8. doi: 10.1038/srep15785

Bryan, C. J., & Sherburn, S. (1999). Seismicity associated with the 1995–1996 eruptions of Ruapehu volcano, New Zealand: narrative and insights into physical processes. *Journal of Volcanology and Geothermal Research*, *90*, 1–8.

Byrdina, S., Grandis, H., Sumintadireja, P., Caudron, C., Syahbana, D. K., Naffrechoux, E., … Vandemeulebrouck, J. (2018). Structure of the acid hydrothermal system of Papandayan volcano, Indonesia, investigated by geophysical methods. *Journal of Volcanology and Geothermal Research*, *358*, 77–86. Retrieved from `https://doi.org/10.1016/j.jvolgeores.2018.06.008` doi: 10.1016/j.jvolgeores.2018.06.008

Cai, Y., & Wang, C. Y. (2005). Fast finite-element calculation of gravity anomaly in complex geological regions. *Geophysical Journal International*, *162*(3), 696–708. doi: 10.1111/j.1365-246X.2005.02711.x

Cheng, C. H., & Johnston, D. (1981). Dynamic and static moduli. , *8*(1), 39–42.

Christenson, B. W. (1994). Convection and stratification in Ruapehu Crater Lake, New Zealand: Implications for Lake Nyos-type gas release eruptions. *Geochemical Journal*, *28*(3), 185–197. doi: 10.2343/geochemj.28.185

Christenson, B. W. (2000). Geochemistry of fluids associated with the 1995-1996 eruption of Mt. Ruapehu, New Zealand: Signatures and processes in the magmatic-hydrothermal system. *Journal of Volcanology and Geothermal Research*, *97*(1-4), 1–30. doi: 10.1016/S0377-0273(99)00167-5

Christenson, B. W., Reyes, A. G., Young, R., Moebis, A., Sherburn, S., Cole-Baker, J., & Britten, K. (2010). Cyclic processes and factors leading to phreatic eruption events: Insights from the 25 September 2007 eruption through Ruapehu Crater Lake, New Zealand. *Journal of Volcanology and Geothermal Research*, *191*(1-2), 15–32. Retrieved from `http://dx.doi.org/10.1016/j.jvolgeores.2010.01.008` doi: 10.1016/j.jvolgeores.2010.01.008

Christenson, B. W., & Wood, C. P. (1993). Evolution of a vent-hosted hydrothermal system beneath Ruapehu Crater Lake, New Zealand. *Bulletin of Volcanology*, *55*(8), 547–565. doi: 10.1007/BF00301808

Coco, A., Currenti, G., Del Negro, C., & Russo, G. (2014). A second order finite-difference ghost-point method for elasticity problems on unbounded domains with applications to volcanology. *Communications in Computational Physics*, *16*(4), 983–1009. doi: 10.4208/cicp.210713.010414a

Coco, A., Currenti, G., Gottsmann, J., Russo, G., & Del Negro, C. (2016). A hydro-geophysical simulator for fluid and mechanical processes in volcanic areas. *Journal of Mathematics in Industry*, *6*(1). Retrieved from `http://dx.doi.org/10.1186/s13362-016-0020-x` doi: 10.1186/s13362-016-0020-x

Coco, A., Gottsmann, J., Whitaker, F., Rust, A., Currenti, G., Jasim, A., & Bunney, S. (2016). Numerical models for ground deformation and gravity changes during volcanic unrest: Simulating the hydrothermal system dynamics of a restless caldera. *Solid Earth*, *7*(2), 557–577. doi: 10.5194/se-7-557-2016

Coco, A., & Russo, G. (2013). Finite-difference ghost-point multigrid methods on Cartesian grids for elliptic problems in arbitrary domains. *Journal of Computational Physics*, *241*, 464–501. Retrieved from `http://dx.doi.org/10.1016/j.jcp.2012.11.047` doi: 10.1016/j.jcp.2012.11.047

Cole, J. W. (1990). Structural control and origin of volcanism in the Taupo volcanic zone, New Zealand. *Bulletin of Volcanology*, *52*(6), 445–459. doi: 10.1007/BF00268925

Conway, C. E., Chamberlain, K. J., Harigane, Y., Morgan, D. J., & Wilson, C. J. (2020). Rapid assembly of high-Mg andesites and dacites by magma mixing at a continental arc stratovolcano. *Geology*, *48*(10), 1033–1037. doi: 10.1130/G47614.1

Corwin, R. F., & Hoover, D. B. (1979). The self-potential method in geothermal exploration. *Geophysics*, *44*(2), 226–245. doi: https://doi.org/10.1190/1.1440964

Crespy, A., Revil, A., Linde, N., Byrdina, S., Jardani, A., Bolève, A., & Henry, P. (2008). Detection and localization of hydromechanical disturbances in a sandbox using the self-potential method. *Journal of Geophysical Research: Solid Earth*, *113*(B1), 1–23. doi: 10.1029/2007JB005042

Currenti, G. (2014). Numerical evidence enabling reconciliation of gravity and height changes in volcanic areas. *Geophysical Journal International*, *197*(1), 164–173. doi: 10.1093/gji/ggt507

Currenti, G., & Napoli, R. (2017). Learning about hydrothermal volcanic activity by modeling induced geophysical changes. *Frontiers in Earth Science*, *5*(May), 1–12. doi: 10.3389/feart.2017.00041

Currenti, G., Napoli, R., Coco, A., & Privitera, E. (2017). Effects of hydrothermal unrest on stress and deformation: insights from numerical modeling and application to Vulcano Island (Italy). *Bulletin of Volcanology*, *79*(4). doi: 10.1007/s00445-017-1110-3

Currenti, G., & Williams, C. A. (2014). Numerical modeling of deformation and stress fields around a magma chamber: Constraints on failure conditions and rheology. *Physics of the Earth and Planetary Interiors*, *226*, 14–27. Retrieved from `http://dx.doi.org/10.1016/j.pepi.2013.11.003` doi: 10.1016/j.pepi.2013.11.003

Del Negro, C., Currenti, G., & Scandura, D. (2009). Temperature-dependent viscoelastic modeling of ground deformation: Application to Etna volcano during the 1993-1997 inflation period. *Physics of the Earth and Planetary Interiors*, *172*(3-4), 299–309. doi: 10.1016/j.pepi.2008.10.019

Fetter, C. W. (2013). *Applied Hydrogeology* (Fourth ed.). Pearson Education Limited.

Fitterman, D. V., & Corwin, R. F. (1982). Inversion of self-potential data from the Cerro Prieto geothermal field, Mexico. *Geophysics*, *47*(6), 938–945. doi: 10.1190/1.1441361

Fournier, N., & Chardot, L. (2012). Understanding volcano hydrothermal unrest from geodetic observations: Insights from numerical modeling and application to White Island volcano, New Zealand. *Journal of Geophysical Research B: Solid Earth*, *117*(11), 1–16. doi: 10.1029/2012JB009469

Fung, Y. C. (1965). *Foundations of Solid Mechanics* (Y. C. Fung, Ed.). Prentice-Hall, Inc. Englewood Cliffs, New Jersey.

Gamble, J. A., Price, R. C., Smith, I. E., McIntosh, W. C., & Dunbar, N. W. (2003). 40Ar/39Ar geochronology of magmatic activity, magma flux and hazards at Ruapehu volcano, Taupo Volcanic Zone, New Zealand. *Journal of Volcanology and Geothermal Research*, *120*(3-4), 271–287. doi: 10.1016/S0377-0273(02)00407-9

Gamble, J. A., Wood, C. P., Price, R. C., Smith, I. E., Stewart, R. B., & Waight, T. (1999). A fifty year perspective of magmatic evolution on Ruapehu

Volcano, New Zealand: Verification of open system behaviour in an arc volcano. *Earth and Planetary Science Letters*, *170*(3), 301–314. doi: 10.1016/S0012-821X(99)00106-5

Giggenbach, W. F., & Glover, R. B. (1975). The use of chemical indicators in the surveillance of volcanic activity affecting the Crater Lake on Mt Ruapehu, New Zealand. *Bulletin Volcanologique*, *39*(1), 70–81. doi: 10.1007/BF02596947

Gottsmann, J., Berrino, G., Rymer, H., & Williams-Jones, G. (2003). Hazard assessment during caldera unrest at the Campi Flegrei, Italy: A contribution from gravity-height gradients. *Earth and Planetary Science Letters*, *211*(3-4), 295–309. doi: 10.1016/S0012-821X(03)00225-5

Gottsmann, J., Biggs, J., Lloyd, R., Biranhu, Y., & Lewi, E. (2020). Ductility and Compressibility Accommodate High Magma Flux Beneath a Silicic Continental Rift Caldera: Insights From Corbetti Caldera (Ethiopia). *Geochemistry, Geophysics, Geosystems*, *21*(4), 1–19. doi: https://doi.org/10.1029/2020GC008952

Gottsmann, J., Camacho, A. G., Martí, J., Wooller, L., Fernández, J., García, A., & Rymer, H. (2008). Shallow structure beneath the Central Volcanic Complex of Tenerife from new gravity data: Implications for its evolution and recent reactivation. *Physics of the Earth and Planetary Interiors*, *168*(3-4), 212–230. doi: 10.1016/j.pepi.2008.06.020

Gottsmann, J., Flynn, M., & Hickey, J. (2020). The transcrustal magma reservoir beneath Soufrière Hills Volcano, Montserrat: insights from 3-D geodetic inversions. *Geophysical Research Letters*, *47*(20), 1–10. doi: 10.1029/2020gl089239

Grobbe, N., & Barde-Cabusson, S. (2019). Self-Potential Studies in Volcanic Environments: A Cheap and Efficient Method for Multiscale Fluid-Flow Investigations. *International Journal of Geophysics*, *2019*(2985824). doi: https://doi.org/10.1155/2019/2985824

Gudmundsson, A. (1983). Stress estimates from the length/width ratios of fractures. *Journal of Structural Geology*, *5*(6), 623–626. doi: 10.1016/0191-8141(83)90075-5

Gudmundsson, A. (1987). Formation and mechanics of magma reservoirs in Iceland. *Geophysical Journal of the Royal Astronomical Society*, *91*(1), 27–41. doi: 10.1111/j.1365-246X.1987.tb05211.x

Gudmundsson, A. (2006). How local stresses control magma-chamber ruptures, dyke injections, and eruptions in composite volcanoes. *Earth-Science Reviews*, *79*(1-2), 1–31. doi: 10.1016/j.earscirev.2006.06.006

Gudmundsson, A. (2011). *Rock Fractures in Geological Processes.* Cambridge University Press. doi: https://doi.org/10.1017/CBO9780511975684

Gudmundsson, A. (2012). Magma chambers: Formation, local stresses, excess pressures, and compartments. *Journal of Volcanology and Geothermal Research*, *237-238*, 19–41. Retrieved from `http://dx.doi.org/10.1016/j.jvolgeores.2012.05.015` doi: https://doi.org/10.1016/j.jvolgeores.2012.05.015

Head, M., Hickey, J., Gottsmann, J., & Fournier, N. (2019). The Influence of Viscoelastic Crustal Rheologies on Volcanic Ground Deformation: Insights From Models of Pressure and Volume Change. *Journal of Geophysical Research: Solid Earth*, *124*(8), 8127–8146. doi: 10.1029/2019JB017832

Head, M., Hickey, J., Gottsmann, J., & Fournier, N. (2021). Exploring the Impact of Thermally Controlled Crustal Viscosity on Volcanic Ground Deformation. *Journal of Geophysical Research: Solid Earth*, *126*(8), 1–22. doi: 10.1029/2020JB020724

Heap, M. J., Kennedy, B. M., Farquharson, J. I., Ashworth, J., Mayer, K., Letham-Brake, M., ... Dingwell, D. B. (2017). A multidisciplinary approach to quantify the permeability of the Whakaari/White Island volcanic hydrothermal system (Taupo Volcanic Zone, New Zealand). *Journal of Volcanology and Geothermal Research*, *332*, 88–108. Retrieved from `http://dx.doi.org/`

10.1016/j.jvolgeores.2016.12.004 doi: 10.1016/j.jvolgeores.2016.12.004

Heap, M. J., Kushnir, A. R., Vasseur, J., Wadsworth, F. B., Harlé, P., Baud, P., ... Deegan, F. M. (2020). The thermal properties of porous andesite. *Journal of Volcanology and Geothermal Research*, *398*. doi: 10.1016/j.jvolgeores.2020.106901

Heap, M. J., Villeneuve, M., Albino, F., Farquharson, J. I., Brothelande, E., Amelung, F., ... Baud, P. (2020). Towards more realistic values of elastic moduli for volcano modelling. *Journal of Volcanology and Geothermal Research*, *390*, 106684. Retrieved from https://doi.org/10.1016/j.jvolgeores.2019.106684 doi: 10.1016/j.jvolgeores.2019.106684

Hickey, J., & Gottsmann, J. (2014). Benchmarking and developing numerical Finite Element models of volcanic deformation. *Journal of Volcanology and Geothermal Research*, *280*, 126–130. doi: 10.1016/j.jvolgeores.2014.05.011

Hickey, J., Gottsmann, J., & Del Potro, R. (2013). The large-scale surface uplift in the Altiplano-Puna region of Bolivia: A parametric study of source characteristics and crustal rheology using finite element analysis. *Geochemistry, Geophysics, Geosystems*, *14*(3). doi: 10.1002/ggge.20057

Hickey, J., Gottsmann, J., Nakamichi, H., & Iguchi, M. (2016). Thermomechanical controls on magma supply and volcanic deformation: Application to Aira caldera, Japan. *Scientific Reports*, *6*(March), 1–10. Retrieved from 10.1038/srep32691 doi: 10.1038/srep32691

Houghton, B. F., Latter, J. H., & Hackett, W. R. (1987). Volcanic hazard assessment for Ruapehu composite volcano, taupo volcanic zone, New Zealand. *Bulletin of Volcanology*, *49*(6), 737–751. doi: 10.1007/BF01079825

Hurst, A. W. (1998). Shallow seismicity beneath Ruapehu Crater Lake: results of a 1994 seismometer deployment. *Bulletin of Volcanology*, *60*(1), 1–9. doi: 10.1007/s004450050212

Hurst, A. W., Bibby, H. M., Scott, B. J., & McGuinness, M. J. (1991). The heat source of Ruapehu crater lake; deductions from the energy and mass balances. *Journal of Volcanology and Geothermal Research*, *46*(1-2), 1–20. doi: 10.1016/0377-0273(91)90072-8

Hurst, A. W., & Dibble, R. R. (1981). Bathymetry, heat output and convection in Ruapehu Crater Lake, New Zealand. *Journal of Volcanology and Geothermal Research*, *9*(2-3), 215–236. doi: 10.1016/0377-0273(81)90005-6

Hutnak, M., Hurwitz, S., Ingebritsen, S. E., & Hsieh, P. A. (2009). Numerical models of caldera deformation: Effects of multiphase and multicomponent hydrothermal fluid flow. *Journal of Geophysical Research: Solid Earth*, *114*(4), 1–11. doi: 10.1029/2008JB006151

Ikard, S. J., & Revil, A. (2014). Self-potential monitoring of a thermal pulse advecting through a preferential flow path. *Journal of Hydrology*, *519*(PA), 34–49. Retrieved from http://dx.doi.org/10.1016/j.jhydrol.2014.07.001 doi: 10.1016/j.jhydrol.2014.07.001

Ingham, M. R., Bibby, H. M., Heise, W., Jones, K. A., Cairns, P., Dravitzki, S., ... Ogawa, Y. (2009). A magnetotelluric study of Mount Ruapehu volcano, New Zealand. *Geophysical Journal International*, *179*(2), 887–904. doi: 10.1111/j.1365-246X.2009.04317.x

Jasim, A., Whitaker, F. F., & Rust, A. C. (2015). Impact of channelized flow on temperature distribution and fluid flow in restless calderas: Insight from Campi Flegrei caldera, Italy. *Journal of Volcanology and Geothermal Research*, *303*, 157–174. doi: 10.1016/j.jvolgeores.2015.07.029

Jolly, A. D., Sherburn, S., Jousset, P., & Kilgour, G. (2010). Eruption source processes derived from seismic and acoustic observations of the 25 September 2007 Ruapehu eruption-North Island, New Zealand. *Journal of Volcanology and Geothermal Research*, *191*(1-2), 33–45. Retrieved from http://dx.doi.org/10.1016/j.jvolgeores.2010.01.009 doi: 10.1016/j.jvolgeores.2010.01.009

Jones, K. A., Ingham, M. R., & Bibby, H. M. (2008). The hydrothermal vent system of Mount Ruapehu, New Zealand - a high frequency MT survey of the summit plateau. *Journal of Volcanology and Geothermal Research*, *176*(4), 591–600. doi: 10.1016/j.jvolgeores.2008.05.006

Kilgour, G., Manville, V., Pasqua, F. D., Graettinger, A., Hodgson, K., & Jolly, G. (2010). The 25 September 2007 eruption of Mount Ruapehu, New Zealand: Directed ballistics, surtseyan jets, and ice-slurry lahars. *Journal of Volcanology and Geothermal Research*, *191*(1-2), 1–14. Retrieved from `http://dx.doi.org/10.1016/j.jvolgeores.2009.10.015` doi: 10.1016/j.jvolgeores.2009.10.015

Kilgour, G. N., Blundy, J. D., Cashman, K., & Mader, H. M. (2013). Small volume andesite magmas and melt-mush interactions at Ruapehu, New Zealand: Evidence from melt inclusions. *Contributions to Mineralogy and Petrology*, *166*(2), 371–392. doi: 10.1007/s00410-013-0880-7

Kilgour, G. N., Saunders, K. E., Blundy, J. D., Cashman, K. V., Scott, B. J., & Miller, C. A. (2014). Timescales of magmatic processes at Ruapehu volcano from diffusion chronometry and their comparison to monitoring data. *Journal of Volcanology and Geothermal Research*, *288*, 62–75. Retrieved from `http://dx.doi.org/10.1016/j.jvolgeores.2014.09.010` doi: 10.1016/j.jvolgeores.2014.09.010

Leonard, G. S., Cole, R. P., Christenson, B. W., Conway, C. E., Cronin, S. J., Gamble, J. A., ... Wilson, C. J. (2021). Ruapehu and Tongariro stratovolcanoes: a review of current understanding. *New Zealand Journal of Geology and Geophysics*, *64*(2-3), 389–420. Retrieved from `https://doi.org/10.1080/00288306.2021.1909080` doi: 10.1080/00288306.2021.1909080

Lisowski, M. (2006). Analytical volcano deformation source models. In P. Blondel (Ed.), *Volcano deformation* (pp. 279–304). Chichester, UK: Springer-Verlag Berlin Heidelberg. doi: 10.1007/978-3-540-49302-0{_}8

Mahardika, H., Revil, A., & Jardani, A. (2012). Waveform joint inversion of seismograms and electrograms for moment tensor characterization of fracking events. *Geophysics*, *77*(5). doi: 10.1190/geo2012-0019.1

Males, K., & Gottsmann, J. (2021). Minimum Detectable Mass and Volume Fluxes During Magmatic Recharge at High Prominence Volcanoes: An Application to Erciyes Dağ Volcano (Turkey). *Frontiers in Earth Science*, *9*(October), 1–17. doi: 10.3389/feart.2021.750063

McTigue, D. F. (1986). Thermoelastic Response of Fluid-Saturated Porous Rock. , *91*(B9), 9533–9542.

Mielke, P., Weinert, S., Bignall, G., & Sass, I. (2016). Thermo-physical rock properties of greywacke basement rock and intrusive lavas from the Taupo Volcanic Zone, New Zealand. *Journal of Volcanology and Geothermal Research*, *324*(June), 179–189. Retrieved from `http://dx.doi.org/10.1016/j.jvolgeores.2016.06.002` doi: 10.1016/j.jvolgeores.2016.06.002

Miller, C., & Jolly, A. (2014). A model for developing best practice volcano monitoring: A combined threat assessment, consultation and network effectiveness approach. *Natural Hazards*, *71*(1), 493–522. doi: 10.1007/s11069-013-0928-z

Miller, C. A., Schaefer, L., Kereszturi, G., & Fournier, D. (2020). Three-Dimensional Mapping of Mt. Ruapehu Volcano, New Zealand, From Aeromagnetic Data Inversion and Hyperspectral Imaging. *Journal of Geophysical Research: Solid Earth*, *125*(2), 1–24. doi: 10.1029/2019JB018247

Miller, V., Hurst, T., & Beavan, J. (2003). Feasibility study for geodetic monitoring of Mt Ruapehu volcano, New Zealand, using GPS. *New Zealand Journal of Geology and Geophysics*, *46*(1), 41–46. doi: 10.1080/00288306.2003.9514994

Mordensky, S. P., Villeneuve, M. C., Kennedy, B. M., Heap, M. J., Gravley, D. M., Farquharson, J. I., & Reuschlé, T. (2018). Physical and mechanical property relationships of a shallow intrusion and volcanic host rock, Pinnacle

Ridge, Mt. Ruapehu, New Zealand. *Journal of Volcanology and Geothermal Research*, *359*, 1–20. Retrieved from https://doi.org/10.1016/j.jvolgeores.2018.05.020 doi: 10.1016/j.jvolgeores.2018.05.020

Mordret, A., Jolly, A. D., Duputel, Z., & Fournier, N. (2010). Monitoring of phreatic eruptions using Interferometry on Retrieved Cross-Correlation Function from Ambient Seismic Noise: Results from Mt. Ruapehu, New Zealand. *Journal of Volcanology and Geothermal Research*, *191*(1-2), 46–59. Retrieved from http://dx.doi.org/10.1016/j.jvolgeores.2010.01.010 doi: 10.1016/j.jvolgeores.2010.01.010

Nairn, I. A., Wood, C. P., Hewson, C. A., & Otway, P. M. (1979). Phreatic eruptions of Ruapehu: April 1975. *New Zealand Journal of Geology and Geophysics*, *22*(2), 155–170. doi: 10.1080/00288306.1979.10424215

Nakagawa, M., Wada, K., Thordarson, T., Wood, C. P., & Gamble, J. A. (1999). Petrologic investigations of the 1995 and 1996 eruptions of Ruapehu volcano, New Zealand: Formation of discrete and small magma pockets and their intermittent discharge. *Bulletin of Volcanology*, *61*(1-2), 15–31. doi: 10.1007/s004450050259

Nakagawa, M., Wada, K., & Wood, C. (2002). Mixed Magmas, Mush Chambers and Eruption Triggers: Evidence from Zoned Clinopyroxene Phenocrysts in Andesitic Scoria from the 1995 Eruptions of Ruapehu Volcano, New Zealand. *Journal of Petrology*, *43*(12), 2279–2303. doi: 10.1093/petrology/43.12.2279

Neuzil, C. E. (2003). Hydromechanical coupling in geologic processes. *Hydrogeology Journal*, *11*(1), 41–83. doi: 10.1007/s10040-002-0230-8

Newhall, C. G., Albano, S. E., Matsumoto, N., & Sandoval, T. (2001). Roles of groundwater in volcanic unrest. *J. Geol. Soc. Phil.*, *56*, 69–84.

Pruess, K., Oldenburg, C., & Moridis, G. (1999). *TOUGH2 USER'S GUIDE , VERSION 2* (Tech. Rep.). Earth Sciences Division, Lawrence Berkeley National Laboratory University of California, Berkeley, California 94720 November.

Raziperchikolaee, S., Singh, V., & Kelley, M. (2020). The effect of Biot coefficient and elastic moduli stress–pore pressure dependency on poroelastic response to fluid injection: laboratory experiments and geomechanical modeling. *Greenhouse Gases: Science and Technology*, *10*(5), 980–998. doi: 10.1002/ghg.2019

Reinsch, T., Dobson, P., Asanuma, H., Huenges, E., Poletto, F., & Sanjuan, B. (2017). Utilizing supercritical geothermal systems: a review of past ventures and ongoing research activities. *Geothermal Energy*, *5*(1). doi: 10.1186/s40517-017-0075-y

Revil, A., & Florsch, N. (2010). Determination of permeability from spectral induced polarization in granular media. *Geophysical Journal International*, *181*(3), 1480–1498. doi: 10.1111/j.1365-246X.2010.04573.x

Revil, A., & Jardani, A. (2013). Application to hydrothermal systems. In *The self-potential method* (pp. 245–283). doi: 10.1017/cbo9781139094252.009

Revil, A., Karaoulis, M., Johnson, T., & Kemna, A. (2012). Review: Some low-frequency electrical methods for subsurface characterization and monitoring in hydrogeology. *Hydrogeology Journal*, *20*, 617–658. doi: 10.1007/s10040-011-0819-x

Revil, A., & Mahardika, H. (2013). Coupled hydromechanical and electromagnetic disturbances in unsaturated porous materials. *Water Resources Research*, *49*(2), 744–766. doi: 10.1002/wrcr.20092

Revil, A., Naudet, V., Nouzaret, J., & Pessel, M. (2003). Principles of electrography applied to self-potential electrokinetic sources and hydrogeological applications. *Water Resources Research*, *39*(5), 1114. doi: 10.1029/2001WR000916

Revil, A., & Pezard, P. A. (1998). Streaming electrical potential anomaly along faults in geothermal areas. *Geophysical Research Letters*, *25*(16), 3197–3200.

Revil, A., Pezard, P. A., & Glover, P. W. J. (1999). Streaming potential in porous media: 1. Theory of the zeta potential. *Journal of Geophysical Research: Solid*

Earth, *104*(B9), 20021–20031. doi: 10.1029/1999jb900089
Revil, A., Saracco, G., & Labazuy, P. (2003). The volcano-electric effect. *Journal of Geophysical Research: Solid Earth*, *108*(B5), 5–1. doi: 10.1029/2002jb001835
Revil, A., Schwaeger, H., Cathles, L. M., & Manhardt, P. D. (1999). Streaming potential in porous media: 2. Theory and application to geothermal systems. *Journal of Geophysical Research: Solid Earth*, *104*(B9), 20033–20048. doi: 10.1029/1999jb900090
Rice, J. R., & Cleary, M. P. (1976). Some Basic Stress Diffusion Solutions for Fluid-Saturated Elastic Porous Media With Compressible Constituents. *REVIEWS OF GEOPHYSICS AND SPACE PHYSICS*, *14*(2), 227–241.
Rinaldi, A. P., Todesco, M., Vandemeulebrouck, J., Revil, A., & Bonafede, M. (2011). Electrical conductivity, ground displacement, gravity changes, and gas flow at Solfatara crater (Campi Flegrei caldera, Italy): Results from numerical modeling. *Journal of Volcanology and Geothermal Research*, *207*(3-4), 93–105. Retrieved from `http://dx.doi.org/10.1016/j.jvolgeores.2011.07.008` doi: 10.1016/j.jvolgeores.2011.07.008
Rizzo, E., Suski, B., Revil, A., Straface, S., & Troisi, S. (2004). Self-potential signals associated with pumping tests experiments. *Journal of Geophysical Research: Solid Earth*, *109*(B10), 1–14. doi: 10.1029/2004JB003049
Rouwet, D., Sandri, L., Marzocchi, W., Gottsmann, J., Selva, J., Tonini, R., & Papale, P. (2014). Recognizing and tracking volcanic hazards related to non-magmatic unrest: A review. *Journal of Applied Volcanology*, *3*(1), 1–17. doi: 10.1186/s13617-014-0017-3
Rowlands, D. P., White, R. S., & Haines, A. J. (2005). Seismic tomography of the Tongariro Volcanic Centre, New Zealand. *Geophysical Journal International*, *163*(3), 1180–1194. doi: 10.1111/j.1365-246X.2005.02716.x
Rutqvist, J., Wu, Y. S., Tsang, C. F., & Bodvarsson, G. (2002). A modeling approach for analysis of coupled multiphase fluid flow, heat transfer, and deformation in fractured porous rock. *International Journal of Rock Mechanics and Mining Sciences*, *39*(4), 429–442. doi: 10.1016/S1365-1609(02)00022-9
Sherburn, S., Bryan, C. J., Hurst, A. W., Latter, J. H., & Scott, B. J. (1999). Seismicity of Ruapehu volcano , New Zealand , 1971 – 1996 : a review. *Journal of Volcanology and Geothermal Research*, *88*, 225–278.
Shibata, T., & Akita, F. (2001). Precursory changes in well water level prior to the March, 2000 eruption of Usu volcano, Japan. *Geophysical Research Letters*, *28*(9), 1799–1802. doi: 10.1029/2000GL012467
Sill, W. R. (1983). Self-potential modeling from primary flows. *Geophysics*, *48*(1), 76–86. doi: 10.1190/1.1441409
Sparks, R. S., Biggs, J., & Neuberg, J. W. (2012). Monitoring volcanoes. *Science*, *335*, 1310. doi: 10.1126/science.1219485
Stern, T., Smith, E. G., Davey, F. J., & Muirhead, K. J. (1987). Crustal and upper mantle structure of the northwestern North Island, New Zealand, from seismic refraction data. *Geophysical Journal of the Royal Astronomical Society*, *91*(3), 913–936. doi: 10.1111/j.1365-246X.1987.tb01674.x
Stissi, S. C., Napoli, R., Currenti, G., Afanasyev, A., & Montegrossi, G. (2021). Influence of permeability on the hydrothermal system at Vulcano Island (Italy): inferences from numerical simulations. *Earth, Planets and Space*, *73*(1). Retrieved from `https://doi.org/10.1186/s40623-021-01515-z` doi: 10.1186/s40623-021-01515-z
Strehlow, K., Gottsmann, J., Rust, A., Hautmann, S., & Hemmings, B. (2020). The influence of long- And short-term volcanic strain on aquifer pressure: A case study from Soufrière Hills Volcano, Montserrat (W.I.). *Geophysical Journal International*, *223*(2), 1288–1303. doi: 10.1093/gji/ggaa354
Strehlow, K., Gottsmann, J. H., & Rust, A. C. (2015). Poroelastic responses of confined aquifers to subsurface strain and their use for volcano monitoring. *Solid*

Earth, *6*(4), 1207–1229. doi: 10.5194/se-6-1207-2015

Strehlow, K., Sandri, L., Gottsmann, J. H., Kilgour, G., Rust, A. C., & Tonini, R. (2017). Phreatic eruptions at crater lakes: occurrence statistics and probabilistic hazard forecast. *Journal of Applied Volcanology*, *6*(1). Retrieved from http://dx.doi.org/10.1186/s13617-016-0053-2 doi: 10.1186/s13617-016-0053-2

Todesco, M. (2009). Signals from the Campi Flegrei hydrothermal system: Role of a "magmatic" source of fluids. *Journal of Geophysical Research: Solid Earth*, *114*(5), 1–14. doi: 10.1029/2008JB006134

Todesco, M., & Berrino, G. (2005). Modeling hydrothermal fluid circulation and gravity signals at the Phlegraean Fields caldera. *Earth and Planetary Science Letters*, *240*(2), 328–338. doi: 10.1016/j.epsl.2005.09.016

Todesco, M., Rinaldi, A. P., & Bonafede, M. (2010). Modeling of unrest signals in heterogeneous hydrothermal systems. *Journal of Geophysical Research: Solid Earth*, *115*(9), 1–19. doi: 10.1029/2010JB007474

Turcotte, D. L., & Schubert, G. (2002). *Geodynamics* (Second edi ed.). Cambridge University Press. doi: https://doi.org/10.1017/CBO9780511807442

Wang, H. F. (2000). *Theory of Linear Poroelasticity with Applications to Geomechanics and Hydrogeology.* Princeton University Press.

Wauthier, C., Roman, D. C., & Poland, M. P. (2016). Joint analysis of geodetic and earthquake fault-plane solution data to constrain magmatic sources: A case study from Kīlauea Volcano. *Earth and Planetary Science Letters*, *455*, 38–48. Retrieved from http://dx.doi.org/10.1016/j.epsl.2016.09.011 doi: 10.1016/j.epsl.2016.09.011

Xu, T., Spycher, N., & Sonnenthal, E. (2004). *TOUGHREACT User's Guide: A Simulation Program for Non-isothermal Multiphase Reactive Transport in Variably Saturated Geologic Media, version 2.0* (Tech. Rep. No. October). Retrieved from http://esd.lbl.gov/FILES/research/projects/tough/documentation/TOUGHREACT_V2_Users_Guide.pdf doi: 10.2172/834237

Zhan, Y., Gregg, P. M., Le Mével, H., Miller, C. A., & Cardona, C. (2019). Integrating Reservoir Dynamics, Crustal Stress, and Geophysical Observations of the Laguna del Maule Magmatic System by FEM Models and Data Assimilation. *Journal of Geophysical Research: Solid Earth*, *124*(12), 13547–13562. doi: 10.1029/2019JB018681

Zhan, Y., Gregg, P. M., & Lu, Z. (2021). Modeling Magma System Evolution During 2006–2007 Volcanic Unrest of Atka Volcanic Center, Alaska. *Journal of Geophysical Research: Solid Earth*, *126*(2), 1–19. doi: 10.1029/2020JB020158

Zhang, J., Wang, C. Y., Shi, Y., Cai, Y., Chi, W. C., Dreger, D., … Yuan, Y. H. (2004). Three-dimensional crustal structure in central Taiwan from gravity inversion with a parallel genetic algorithm. *Geophysics*, *69*(4), 917–924. doi: 10.1190/1.1778235

Zlotnicki, J. (2015). Dynamics of volcanic eruptions: Understanding electric signatures for activity monitoring. *Comptes Rendus - Geoscience*, *347*(3), 112–123. Retrieved from http://dx.doi.org/10.1016/j.crte.2015.05.003 doi: 10.1016/j.crte.2015.05.003

Zlotnicki, J., & Nishida, Y. (2003). Review on morphological insights of self-potential anomalies on volcanoes. *Surveys in Geophysics*, *24*(4), 291–338. doi: 10.1023/B:GEOP.0000004188.67923.ac